Does the rotational direction of a wind turbine impact the wake in a stably stratified atmospheric boundary layer?

Antonia Englberger[1], Andreas Dörnbrack[1], and Julie K. Lundquist[2,3]

[1]German Aerospace Center, Institute of Atmospheric Physics, Oberpfaffenhofen, Germany
[2]Department of Atmospheric and Oceanic Sciences, University of Colorado Boulder, Boulder, USA
[3]National Renewable Energy Laboratory, Golden, Colorado, USA

Correspondence: Antonia Englberger (antonia.englberger@dlr.de)

Abstract. Stably stratified atmospheric boundary layers are often characterized by a veering wind profile, in which the wind direction changes clockwise with height in the Northern Hemisphere. Wind-turbine wakes respond to this veer in the incoming wind by stretching from a circular shape into an ellipsoid. We investigate the relationship between this stretching and the direction of the turbine rotation by means of large-eddy simulations. Clockwise rotating, counterclockwise rotating, and non-rotating actuator disc turbines are embedded in wind fields with no wind veer or in wind fields with an Ekman spiral representative of the Northern Hemisphere, resulting in six combinations of rotor rotation and inflow wind condition. The impact of the Coriolis force via the Ekman spiral depends on the rotational direction of the actuator disc, whereas the direction of the disc rotation exerts little impact if no veer is present. The differences result from the interaction of the actuator rotation with the Ekman spiral and are present in the zonal, the meridional, and the vertical wind components of the wake. The interaction of the Ekman spiral with both rotational directions lead to two different flow fields characterizing the wake. In the case of a counterclockwise rotating actuator disc, the rotational direction of the wake persists in the whole wake. In case of a clockwise rotating actuator, however, the rotational direction is different in the near wake in comparison to the far wake. The physical mechanism responsible for this difference is explained by a simple linear superposition of the inflow wind field, characterized by vertical wind shear and wind veer, with a wind-turbine model including a Rankine vortex, representing the rotational effects imposed on the flow by the rotating blades.

1 Introduction

In wind energy science, the engineering system of a wind turbine interacts with the geophysical system of the atmospheric boundary layer (ABL). The canonical ABL over land experiences a diurnal cycle in prevailing wind and turbulence conditions (Stull, 1988). The diurnal cycle is driven by shortwave heating during day and longwave radiative cooling at night. Shortwave heating of the surface triggers convective turbulence that mixes throughout the boundary layer, resulting in a well-mixed convective boundary layer (CBL) during day with little vertical wind shear (change of wind speed with height) and high levels of turbulence. At night, radiative cooling of the surface leads to a decay of the convective turbulence, resulting in a stable boundary layer (SBL), with low turbulence levels and highly sheared wind profiles. The interaction between the Coriolis force acting on the velocity components and friction in the boundary layer will cause winds to rotate with height, approaching the geostrophic wind. This veering of the wind through the boundary layer is described by the hemispheric-dependent Ekman spiral. In the Northern Hemisphere, winds rotate clockwise with height (i.e. westerly near the surface and northerly aloft), while in the southern hemisphere, winds rotate counterclockwise with height (i.e. westerly near the surface and southerly aloft). Therefore, the nighttime wind system in the Northern Hemispheric mid-latitudes is typically characterized by a veering wind (a wind that rotates clockwise with height) and a pronounced vertical wind shear (Walter et al., 2009). Of course, synoptic events such as frontal passages or topographically-driven phenomena such as drainage flows can modify this typical background veer.

The stability-dependent wind and turbulence conditions determine the entrainment of energy and momentum into the wake region and the resulting wake structure, with fast-eroding wakes in convective conditions and wakes persisting further downwind in stably stratified conditions which are additionally characterized by a skewed wake (Abkar et al., 2016; Vollmer et al., 2017; Englberger and Dörnbrack, 2018a). This stability dependence has been investigated in numerical simulations for the SBL (Aitken et al., 2014; Bhaganagar and Debnath, 2014, 2015; Dörenkämper et al., 2015), the CBL (Mirocha et al., 2014), both of them (Abkar and Porté-Agel, 2014; Vollmer et al., 2017), or the complete diurnal cycle (Abkar et al., 2016; Englberger and Dörnbrack, 2018a).

The upstream wind and turbulence profiles, characterized by the prevailing atmospheric condition, interact with the rotating blades of a wind turbine. Due to aerodynamics and design of the wind turbine blades, the rotational direction of most industrial wind turbines is clockwise (while looking downwind). Clockwise rotating blades will exhibit a counterclockwise rotating wake (Zhang et al., 2012). Studies investigating the effect of wind turbine rotors rotating in opposite directions, especially, for wind farm optimization, show that the rotational direction has an impact on the wake structure of a wind turbine and, therefore, on the performance of a downwind turbine (Vermeer et al., 2003; Shen et al., 2007; Sanderse, 2009; Kumar et al., 2013; Hu et al., 2013; Yuan et al., 2014; Mühle et al., 2017). Further, in simulations representing an array of wind turbines with a second row rotating opposite to the rotation of the first row, an increase in productivity was found in comparison to the co-rotating pair of turbines. This improvement is related to the different direction of the angular component in the wake and, therefore, the change in the angle of attack on the downwind turbine (Mühle et al., 2017).

These studies, which detect a rotational direction impact on the wake, were performed for wind conditions without significant vertical wind shear and without wind veer in the rotor altitudes. Vertical wind shear and wind veer, however, impact the

wake characteristics (Abkar and Porté-Agel, 2016; Vollmer et al., 2017; Englberger and Dörnbrack, 2018a), and also power production (Sanchez Gomez and Lundquist, 2019a). As both effects influence the wake, their interaction in combination with different rotational directions might have a large impact on the wake characteristics in stably stratified regimes. This possible impact is investigated in this study in detail, aiming to answer the question:

Does the rotational direction of a wind turbine impact the wake in a stably stratified atmospheric boundary layer?

We investigate the relationship between the upstream wind profile and the direction of the turbine rotation by large-eddy simulations (LESs). Clockwise-rotating, counterclockwise-rotating and non-rotating actuator discs are embedded in two different atmospheric regimes. The simplest scenario includes only wind shear, specifically, an increase of wind speed with height. The more complex scenario also includes veer characteristics of the Northern Hemisphere's Ekman spiral, which are representative of a stably stratified ABL. The simulations represent six combinations of rotor rotation and wind conditions as sketched in Fig. 1. To our knowledge, this is the first study which investigates the dependence of wake characteristics on the rotational direction of a rotor and wind veer in a stably stratified ABL.

The paper is organised as follows. The numerical model EULAG, the wind-turbine simulation setup and the metrics are described in Sect. 2. The interaction of rotational direction with wind veer is presented in Sect. 3 and the developed simplified wake model to explain this interaction in Sect. 4. The resulting impact of the rotational direction on the flow in the wake is illustrated in Sect. 5. A conclusion follows in Sect. 6.

2 Numerical Model Framework

2.1 The Numerical Model EULAG

The dry ABL flow through a wind turbine is simulated with the multiscale geophysical flow solver EULAG (Prusa et al., 2008). The acronym EULAG refers to the ability of solving the equations of motion either in an EUlerian (flux form) (Smolarkiewicz and Margolin, 1993) or in a semi-LAGrangian (advective form) (Smolarkiewicz and Pudykiewicz, 1992) mode. The geophysical flow solver EULAG is at least of second-order accurate in time and space (Smolarkiewicz and Margolin, 1998) and well-suited for massively-parallel computations (Prusa et al., 2008). It can be run parallel up to a domain decomposition in three dimensions. A comprehensive description and discussion of the geophysical flow solver EULAG can be found in Smolarkiewicz and Margolin (1998) and Prusa et al. (2008).

For the numerical simulations conducted for this paper, the Boussinesq equations for a flow with constant density ρ_0 = 1.1 kg m^{-3} are solved for the Cartesian velocity components $\mathbf{v} = (u, v, w)$ and for the potential temperature perturbations

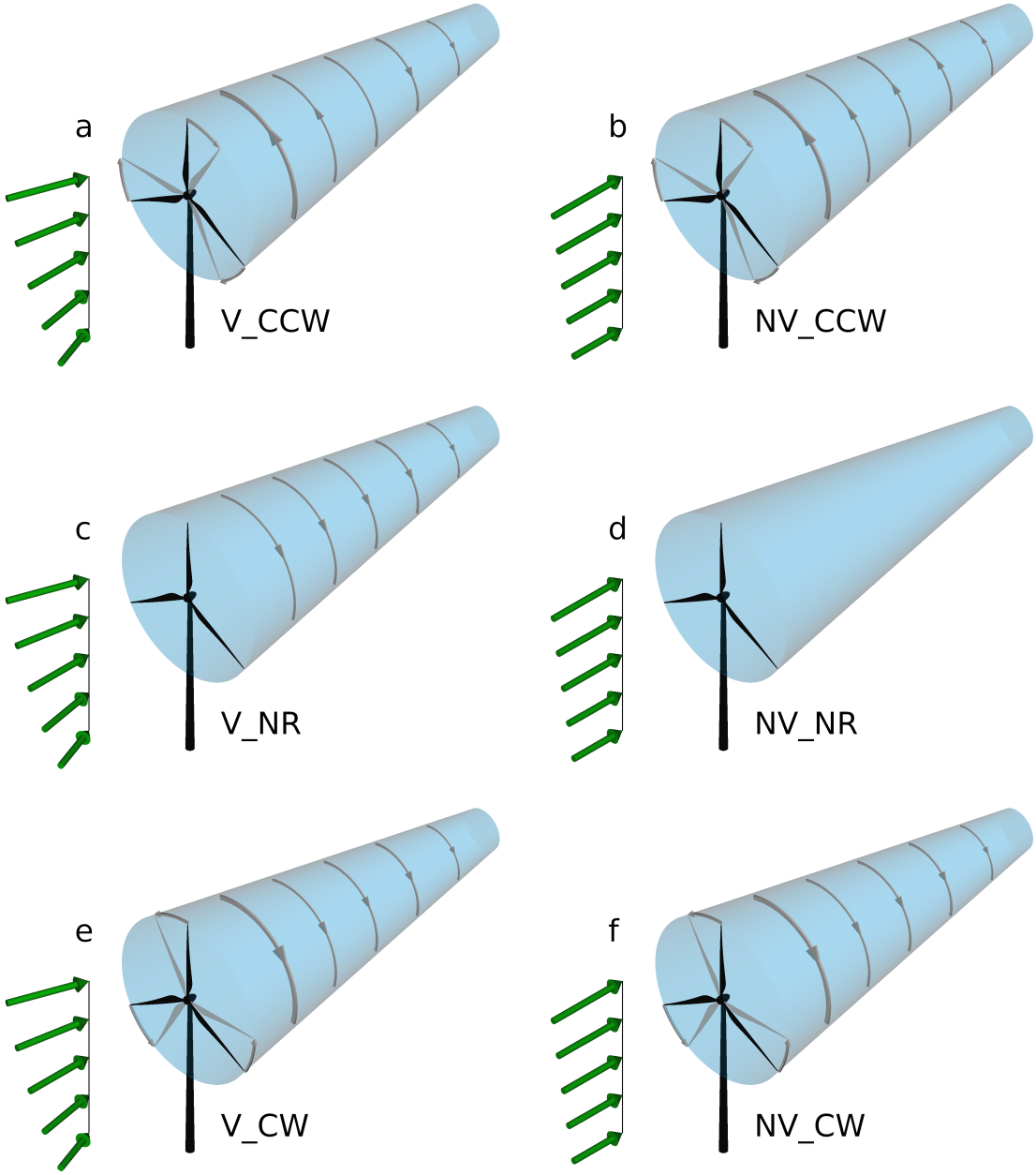

Figure 1. Schematic illustration of the rotational direction of the wake for the cases: Wind veer with clockwise blade rotation (V_CCW) in (a), no wind veer with clockwise blade rotation (NV_CCW) in (b), wind veer with no blade rotation (V_NR) in (c), no wind veer with no blade rotation (NV_NR) in (d), wind veer with counterclockwise blade rotation (V_CW) in (e), no wind veer with counterclockwise blade rotation (NV_CW) in (f).

$\Theta^{'} = \Theta - \Theta_{BL}$ (Smolarkiewicz et al., 2007),

$$\frac{d\mathbf{v}}{dt} = -G\boldsymbol{\nabla}\left(\frac{p^{'}}{\rho_0}\right) + \mathbf{g}\frac{\Theta^{'}}{\Theta_0} + \boldsymbol{\mathcal{V}} + \mathbf{M} + \beta_{\mathbf{v}}\frac{\mathbf{F}_{WT}}{\rho_0} - 2\Omega(\mathbf{v} - \mathbf{v}_{BL}), \tag{1}$$

$$\frac{d\Theta^{'}}{dt} = -\mathbf{v}\cdot\nabla\Theta_{BL} + \mathcal{H}, \tag{2}$$

$$\boldsymbol{\nabla}\cdot(\rho_0\mathbf{v}) = 0, \tag{3}$$

where Θ_0 = 300 K represents the constant reference value. Height dependent ABL states u_{BL}(z), v_{BL}(z), w_{BL}(z), and Θ_{BL}(z) enter Eqs. 1 - 3 in the buoyancy term, the Coriolis term, and as boundary conditions. In Eqs. 1, 2 and 3, d/dt, $\boldsymbol{\nabla}$ and $\boldsymbol{\nabla}\cdot$ represent the total derivative, the gradient and the divergence, respectively. The quantity $p^{'}$ represents the pressure perturbation with respect to the background state and **g** the vector of acceleration due to gravity. The factor G represents geometric terms that result from the general, time-dependent coordinate transformation (Wedi and Smolarkiewicz, 2004; Smolarkiewicz and Prusa, 2005; Prusa et al., 2008; Kühnlein et al., 2012). The subgrid-scale terms $\boldsymbol{\mathcal{V}}$ and $\mathcal{H}$ symbolise viscous dissipation of momentum and diffusion of heat and **M** denotes the inertial forces of coordinate-dependent metric accelerations. $\mathbf{F}_{WT}$ corresponds to the turbine-induced force and the scalar prefactors $\beta_{\mathbf{v}}$ = (1, β_v, β_w) to the rotation of the rotor. The Coriolis force is represented by the angular velocity vector of the Earth's rotation. All following simulations are performed with a TKE closure (Schmidt and Schumann, 1989; Margolin et al., 1999).

2.2 Setup of the Wind-Turbine Simulations

Wind-turbine simulations with open horizontal boundaries are performed for a stably stratified ABL lasting 20 min on $512 \times 64 \times 64$ grid points with a uniform horizontal and vertical resolution of 5 m. The rotor of the wind turbine is located at 300 m in x-direction and centred in y-direction with a diameter (D) and a hub height z_h, both 100 m. In the scope of this paper, we performed six wind-turbine simulations, listed in Table 1 and schematically plotted in Fig. 1. These simulations differ by two main components, the presence of veer and the wake rotation.

All simulations are initialized with the zonal wind profile including vertical wind shear

$$u_{BL}(z) = u_g \cdot \left(1 - exp\left(-\frac{z\sqrt{f/\kappa}}{\sqrt{2}}\right)\right), \tag{4}$$

with a geostrophic wind u_g = 10 m s^{-1}, the Coriolis parameter f = 1.0×10^{-4} s^{-1}, and an eddy viscosity coefficient κ = 0.06 m^2 s^{-1}, following Shapiro and Fedorovich (2010). In the simulations with wind veer V_, the wind direction change over the 100 m rotor disc is 8 ° with $v_{BL}(z_h)$ = 0. The meridional wind profile of the ABL in the veered cases is therefore

$$v_{BL}(z) = u_{BL}(z) \cdot tan\left(\left(270^\circ - \left(262^\circ + 8^\circ\frac{z}{100m}\right)\right)\frac{\pi}{180^\circ}\right) \tag{5}$$

in the lowest 200 m and constant above. A wind veer of 0.08 ° m^{-1} represents a nighttime situation, following Walter et al. (2009) and is in agreement with measurements (Walter et al., 2009; Bodini et al., 2019; Sanchez Gomez and Lundquist, 2019b)

Table 1. List of all performed simulations in this study. Here, V_ refers to veer and NV_ to no veer, CCW to counterclockwise wake rotation, CW to clockwise wake rotation, and NR to no rotation of the disc.

simulation	veer	wake rotation
V_CCW	yes	counterclockwise
V_NR	yes	no
V_CW	yes	clockwise
NV_CCW	no	counterclockwise
NV_NR	no	no
NV_CW	no	clockwise

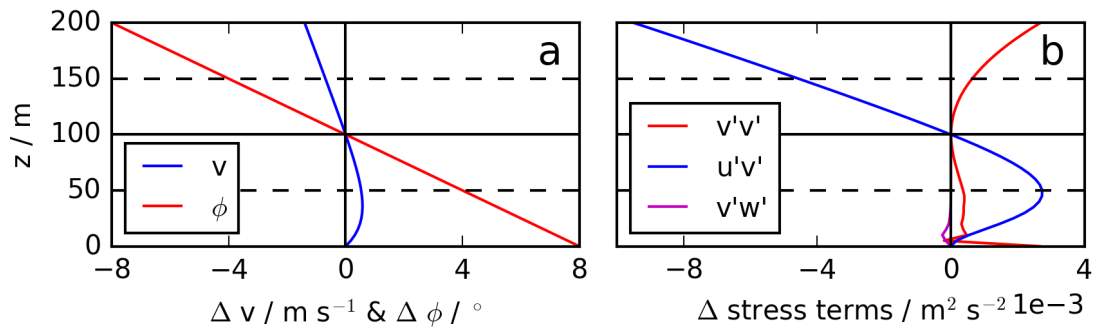

Figure 2. Differences in the initial conditions between V_ and NV_ for the spanwise velocity v and the incoming wind direction Φ, whereas the differences are related to 270°, in (a) and the Reynolds stress tensor terms $v'v'$, $u'v'$ and $v'w'$ in (b).

indicating that a veer in excess of 0.2 ° m^{-1} does occur. In simulations without wind veer NV_, the meridional wind profile is

$$v_{BL}(z) = 0. \tag{6}$$

The differences in the inflow conditions between V_ and NV_ simulations are presented in Fig. 2(a) for the spanwise wind component v and the wind direction ϕ with respect to 270 ° as V_ - NV_. The vertical velocity is

$$w_{BL}(z) = 0 \tag{7}$$

in all simulations. The potential temperature is

$$\Theta_{BL}(z) = \Theta_0 + \frac{3\,K}{200\,m} z \tag{8}$$

in the lowest 200 m and 303 K above.

The parametrization for seeding turbulent velocity perturbations as presented by Englberger and Dörnbrack (2018b) is applied to represent a turbulent stably stratified regime in a wind-turbine simulation with open horizontal boundary conditions. The parametrization considers three 3 D wind fields (u, v, and w), resulting from a neutral ABL precursor simulation, which are modified by a stratification-dependent weighting, resulting from the SBL state of a diurnal cycle precursor simulation. The applied parametrization makes the LESs numerically efficient and computationally fast (about 1 min wall time to simulate 1 min model time on 64 Intel Xeon E5-2697 v3 threads at 2.6 GHz), a feature, which is well suited for this case study. A more detailed description of the parametrization as well as all parameters required to apply the parametrization are described in detail in Englberger and Dörnbrack (2018b).

The ABL flow (Eqs. 4-8) in combination with the impressed turbulence of a stably stratified regime result in exactly the same initial Reynolds stress tensor terms of $u'u'$, $w'w'$, and $u'w'$ in V_ and NV_ whereas there are differences in $v'v'$, $u'v'$, and $v'w'$ (Fig. 2(b)). In the height of the rotor, $u'v'$ is symmetric with respect to hub height and both $u'v'$ and $v'v'$ increase approaching the blade tip, whereas $v'w'$ is marginal.

The axial $\mathbf{F}_x$ and tangential $\mathbf{F}_\Theta$ (Eqs. 9 and 10) turbine-induced forces ($\mathbf{F}_{WT} = \mathbf{F}_x + \mathbf{F}_\Theta$) in Eq. 1 are parametrized with the blade element momentum (BEM) method as rotating actuator disc including a nacelle and excluding the tower.

$$\begin{aligned} |F_x|\big|_{x_0,y,z} &= \frac{1}{2}\rho_0 \frac{Bc}{2\pi r_{x_0,y,z}}(c_L\cos\Phi + c_D\sin\Phi) \\ &\quad \times A_{x_0,y,z}\frac{u^2_{x_\infty,y,z}(1-a)^2}{\sin^2\Phi} \end{aligned} \tag{9}$$

$$\begin{aligned} |F_\Theta|\big|_{x_0,y,z} &= \frac{1}{2}\rho_0 \frac{Bc}{2\pi r_{x_0,y,z}}(c_L\sin\Phi - c_D\cos\Phi) \\ &\quad \times A_{x_0,y,z}\frac{u_{x_\infty,y,z}(1-a)\Omega r_{x_0,y,z}(1+a^{'})}{\sin\Phi\cos\Phi}. \end{aligned} \tag{10}$$

Here, the centre of the rotor in x-direction is defined by the grid-point coordinate x_0. B represents the number of blades, c is the chord length of the blade, c_L is the lift coefficient, c_D is the drag coefficient, Φ is the angle between the plane of rotation and the relative streamwise velocity, a is the axial induction factor, and $a^{'}$ is the tangential induction factor. Following Hansen (2008), we calculate a and $a^{'}$ by an iterative procedure from the airfoil data. For the airfoil data, the 10 MW reference wind turbine from DTU (Bak et al., 2013) is applied, whereas the radius of the rotor as well as the chord length of the blades are scaled to a rotor with a diameter of 100 m. The upstream velocity $u_{x_\infty,y,z}$ is taken at the first upstream grid point in the x-direction and the corresponding y and z coordinates. With the exception of ρ_0 and B, all other parameters appearing in Eqs. 9 and 10 depend on the radius $r_{x_0,y,z}$ and vary spatially. Further, the rotation frequency Ω is set to 7 rpm. A more detailed description of the wind-turbine parametrization and the applied smearing of the forces in the numerical code, as well as all values used in the wind-turbine parametrization can be found in Englberger and Dörnbrack (2017, parametrization B).

Three different wake conditions are considered: Clockwise wake rotation (CW), no wake rotation (NR), and counter-clockwise wake rotation (CCW), defined from a view looking downwind at the wind turbine. In these simulations, only the prefactors β_v and β_w in Eq. 1 differ. A clockwise wake rotation is defined by β_v = -1 and β_w = 1, a counterclockwise wake rotation by β_v = 1 and β_w = -1, and no rotation by β_v = 0 and β_w = 0, with β_u = 1 in each simulation. A clockwise wake ro-

Table 2. List of grid points (gp) considered for the sectors applied in the evaluation. Right and left correspond to the rotor section from a view upwind of the wind turbine on the rotor with radius R.

sector	top tip	right	bottom tip	left
60 °	gp ≤ 30 ° or gp ≥ 330 °	60 ° ≤ gp ≤ 120 °	150 ° ≤ gp ≤ 210 °	240 ° ≤ gp ≤ 300 °
90 °	gp ≤ 45 ° or gp ≥ 315 °	45 ° < gp < 135 °	125 ° ≤ gp ≤ 225 °	225 ° < gp < 315 °

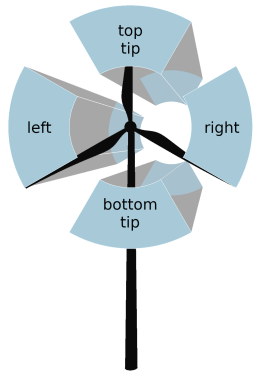

Figure 3. Schematic illustration of the top-tip sector (tt), the bottom-tip sector (bt), as well as the right and left sectors, defined from a view looking downwind toward the wind turbine on the disc. All sectors are 60 ° and 25 m ≤ r ≤ 50 m sectors.

tation is initiated by a counterclockwise blade rotation, due to conservation of angular momentum (e.g. described in Zhang et al. (2012)). We do not simulate the rotor rotation, instead, we exerted the rotor forces directly on the velocity fields (Eq. 1). Therefore, in the following we will refer to different wake rotations, which, however, can be linked directly towards the opposite blade rotation. Most wind turbines rotate in the clockwise direction, resulting in a counterclockwise wake rotation, so the CCW simulations represent the typical situation.

2.3 Metrics

For the investigation of the dependence of wake characteristics on the wake rotation and wind veer, the following characteristics are used: the spatial distribution of the time-averaged streamwise wind component $\overline{u_{i,j,k}}$, the time-averaged spanwise wind component $\overline{v_{i,j,k}}$, the time-averaged vertical wind component $\overline{w_{i,j,k}}$, the streamwise velocity deficit

$$VD_{i,j,k} = \frac{\overline{u_{1,j,k}} - \overline{u_{i,j,k}}}{\overline{u_{1,j,k}}}, \tag{11}$$

and the total turbulence intensity

$$I_{i,j,k} = \frac{\frac{1}{3}\sqrt{\sigma^2_{u_{i,j,k}} + \sigma^2_{v_{i,j,k}} + \sigma^2_{w_{i,j,k}}}}{\overline{u_{i,j,k_h}}}, \tag{12}$$

with $\sigma_{u_{i,j,k}} = \sqrt{\overline{u'^2_{i,j,k}}}$, $\sigma_{v_{i,j,k}} = \sqrt{\overline{v'^2_{i,j,k}}}$, and $\sigma_{w_{i,j,k}} = \sqrt{\overline{w'^2_{i,j,k}}}$, as well as $u'_{i,j,k} = u_{i,j,k} - \overline{u_{i,j,k}}$, $v'_{i,j,k} = v_{i,j,k} - \overline{v_{i,j,k}}$, and $w'_{i,j,k} = w_{i,j,k} - \overline{w_{i,j,k}}$. The indices of the discrete grid points are denoted by $i = 1 \ldots n$, $j = 1 \ldots m$ and $k = 1 \ldots l$ in the x, y and z directions, respectively. These characteristics are averaged over the last 10 min of the corresponding 20 min wind-turbine simulation. The temporal average is calculated online in the numerical model and updated at every timestep according to the method of Fröhlich (2006, Eq. 9.1).

In the following, the quantities $\overline{u_{i,j,k}}$, $\overline{v_{i,j,k}}$, and $\overline{w_{i,j,k}}$ are evaluated and discussed downwind of the wind turbine up to 20 D. Further, the rotor area is divided into four sections of 60 °, referred to hereafter as top tip, right, bottom tip, and left (see Table 2 and Fig. 3). These sectors include radial points with 25 m ≤ r ≤ 50 m, which represent the outer rotor region. We also evaluate the characteristics with 90 ° sectors (Table 2) or for 0 m < r ≤ 50 m representing the whole rotor (excluding nacelle region). The resulting values of all four combinations are comparable between the 60 ° and 90 ° segments, and between the 0 m < r ≤ 50 m and 25 m ≤ r ≤ 50 m sections. As the features are more distinctive for 60 ° and 25 m ≤ r ≤ 50 m sectors, these values are applied for the derivation of the sector characteristics in chapter 4.

3 Interaction of Rotational Direction with Wind Veer

3.1 Impact on the Streamwise Velocity Component

The relationship between wind veer and the direction of the turbine rotation is investigated with x - y cross sections of the streamwise velocity at 100 m hub height (Fig. 4), in the top half of the rotor disc at 125 m (Fig. 5), and in the bottom half of the rotor disc at 75 m (Fig. 6) and also with vertical and spanwise profiles of the velocity deficit VD and the total turbulence intensity I at a downstream distances of 10 D (Figs. 7, 9). The main results of each comparison are listed in Table 3.

In a first step, we compare the two non-rotating simulations with and without veer, V_NR and NV_NR, in Figs. 4(c) vs. (d), 5(c) vs. (d), and 6(c) vs. (d). This comparison reveals the effect of pure wind veer without disc rotation on the wake structure. First, the elongation of the wake is affected by wind veer. The wake at hub height in V_NR (Fig. 4(c)) recovers more rapidly in comparison to NV_NR (Fig. 4(d)). This effect prevails over the whole rotor area in the vertical (Fig. 7(a)) as well as in the spanwise direction (Fig. 7(c), (e), (g)). The inflow total turbulence intensity comparing V_ and NV_ differs only by $v'v'$ (Fig. 2(b), Eq. 12). The resulting enhanced production of turbulent kinetic energy due to shear in V_NR in comparison to NV_NR in the wake region (Fig. 7(b), (d), (f), (h)) results in a larger entrainment of ambient air and, therefore, in the more rapid flow recovery of the wake in V_NR. In addition, the combination of vertical wind shear and wind veer causes a skewed spatial structure in the veered simulation V_NR in Fig. 8(a), which is not prevalent in the non-veered case NV_NR in Fig. 8(b). This skewed structure under veered inflow conditions is similar to those observed in the simulations of Abkar et al. (2016) (Fig. 16), Vollmer et al. (2017) (Fig. 9), and Englberger and Dörnbrack (2018a) (Fig. 6) as well as in measurements of Bodini et al. (2017) (Fig. 12) and Brugger et al. (2019) (Fig. 4).

Second, the wake deflection angle in the top (Fig. 5(c) and (d)) and the bottom half (Fig. 6(c) and (d)) of the rotor disc differs between the veered V_NR and non-veered case NV_NR. The direction of the wake center line is determined by the

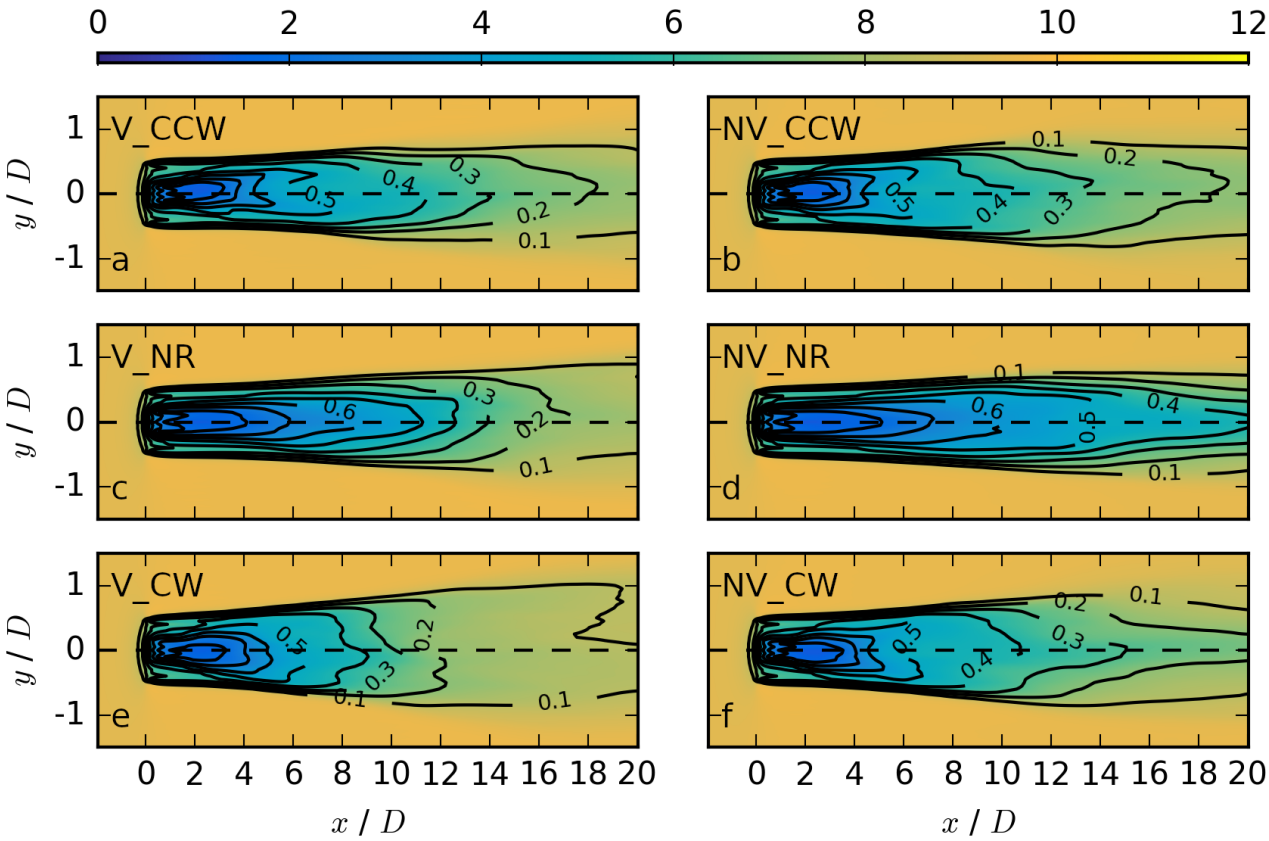

Figure 4. Coloured contours of the streamwise velocity $\overline{u_{i,j,k_h}}$ in m s^{-1} at hub height k_h, averaged over the last 10 min, for V_CCW in (a), NV_CCW in (b), V_NR in (c), NV_NR in (d), V_CW in (e), and NV_CW in (f). The black contours represent the velocity deficit VD_{i,j,k_h} at the same vertical location.

incoming wind direction (Fig. 2(a)), resulting in the opposite behavior between the upper and the lower half of the rotor. Likewise, the upper half of the wake deflects to the south (Figs. 5(c), 8(a)) while the lower half of the wake deflects to the north (Figs. 6(c), 8(a)). In contrast, the wake for NV_NR (Figs. 5(d), 6(d), 8(b)) does not deflect at any altitude due to $v_{BL} = 0$. This difference in the wake deflection angle is responsible for the shift of the maximum at 75 m in Fig. 7(g) towards the south and at 125 m in Fig. 7(c) towards the north, which is not the case at hub height (Fig. 7(e)).

To investigate the effect of wind veer on commonly clockwise rotating wind turbines, we compare V_CCW to NV_CCW, in Figs. 4(a) vs. (b), 5(a) vs. (b), 6(a) vs. (b), and 7. No significant effect of veer appears in wake recovery at hub height (Fig. 4(a) vs. Fig. 4(b). Considering Fig. 7(e), the wake recovers slightly less rapid under veered inflow conditions in comparison to non-veered ones due to a slightly smaller turbulence intensity level in the wake under veered inflow conditions (Fig. 7(f)). This behavior of the recovery rate persists almost over the whole disc in the vertical (Fig. 7(a), (b)).

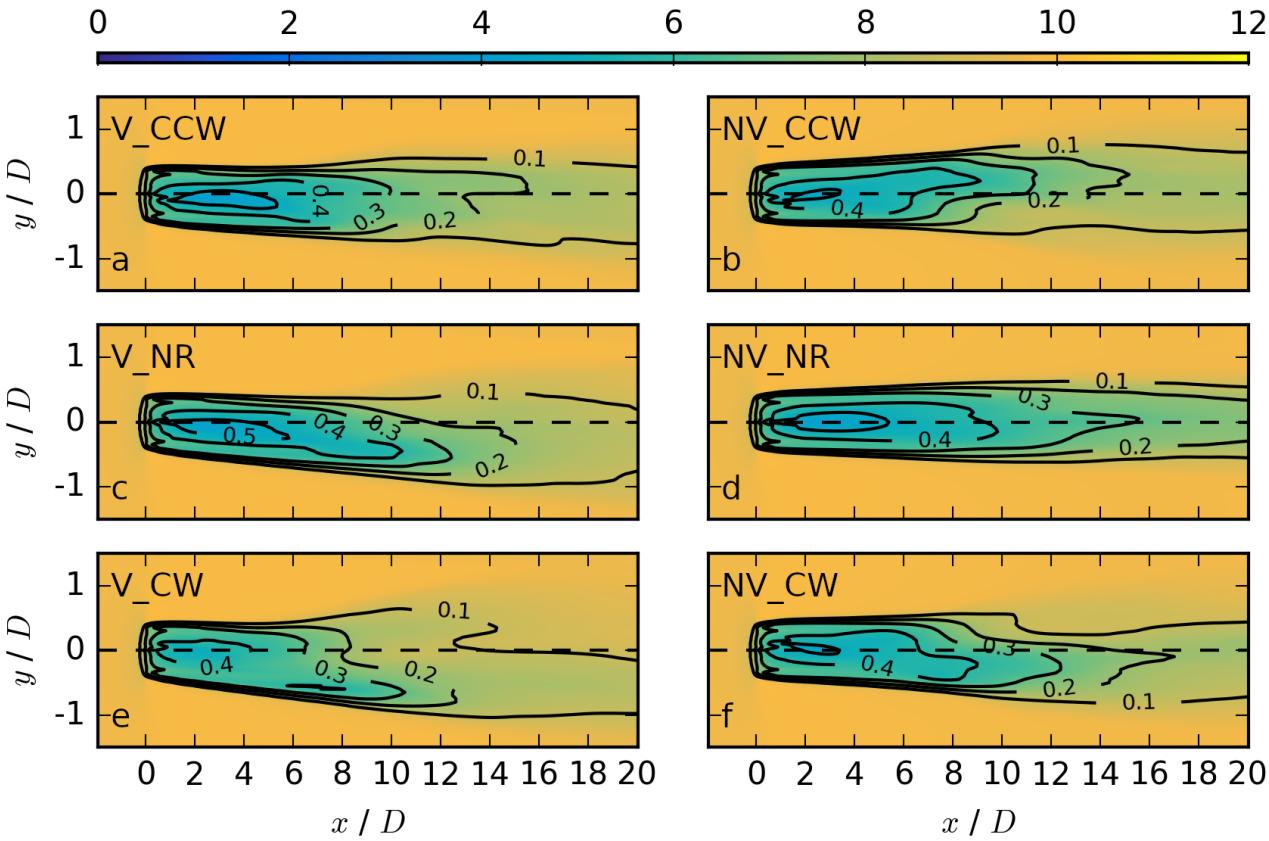

Figure 5. Coloured contours of the streamwise velocity $\overline{u_{i,j,k_*}}$ in m s^{-1} at z = 125 m with index k_*, averaged over the last 10 min, for the same cases as in Fig. 4. The black contours represent the velocity deficit VD_{i,j,k_*} at the same vertical location.

Further, inflow wind veer causes wake deflection in both the top half (Fig. 5(a) vs. Fig. 5(b)) and the bottom half (Fig. 6(a) vs. Fig. 6(b)) of the rotor disc. In the non-veered simulation NV_CCW, the wake is slightly deflected towards the north in the top-tip sector (Fig. 5(b)) and towards the south in the bottom-tip sector (Fig. 6(b)). Compared to the non-deflected wake in NV_NR (Figs. 5(d), 6(d)), this effect is caused by the rotation of the rotor, which transports higher momentum air counterclockwise, resulting in a northward wake deflection at 125 m. Consequently, the opposite situation prevails at 75 m. The wake in the veered simulation V_CCW is deflected towards the south (north) in the upper (lower) rotor part (Fig. 5(a) (Fig. 6(a))), in comparison to the northward (southward) deflected one in NV_CCW (Fig. 5(b) (Fig. 6(b))). The change in the deflection from northward to southward and vice versa results from the interaction of a clockwise blade rotation with the veered inflow conditions and is responsible for the axis-symmetric behavior of ΔVD in Fig. 7(c) and (g).

To further investigate the effect of wind veer on counterclockwise rotating wind turbines, we compare V_CW and NV_CW, in Figs. 4(e) vs. (f), 5(e) vs. (f), 6(e) vs. (f), and 7. Considering counterclockwise rotating blades, the wind veer causes a more

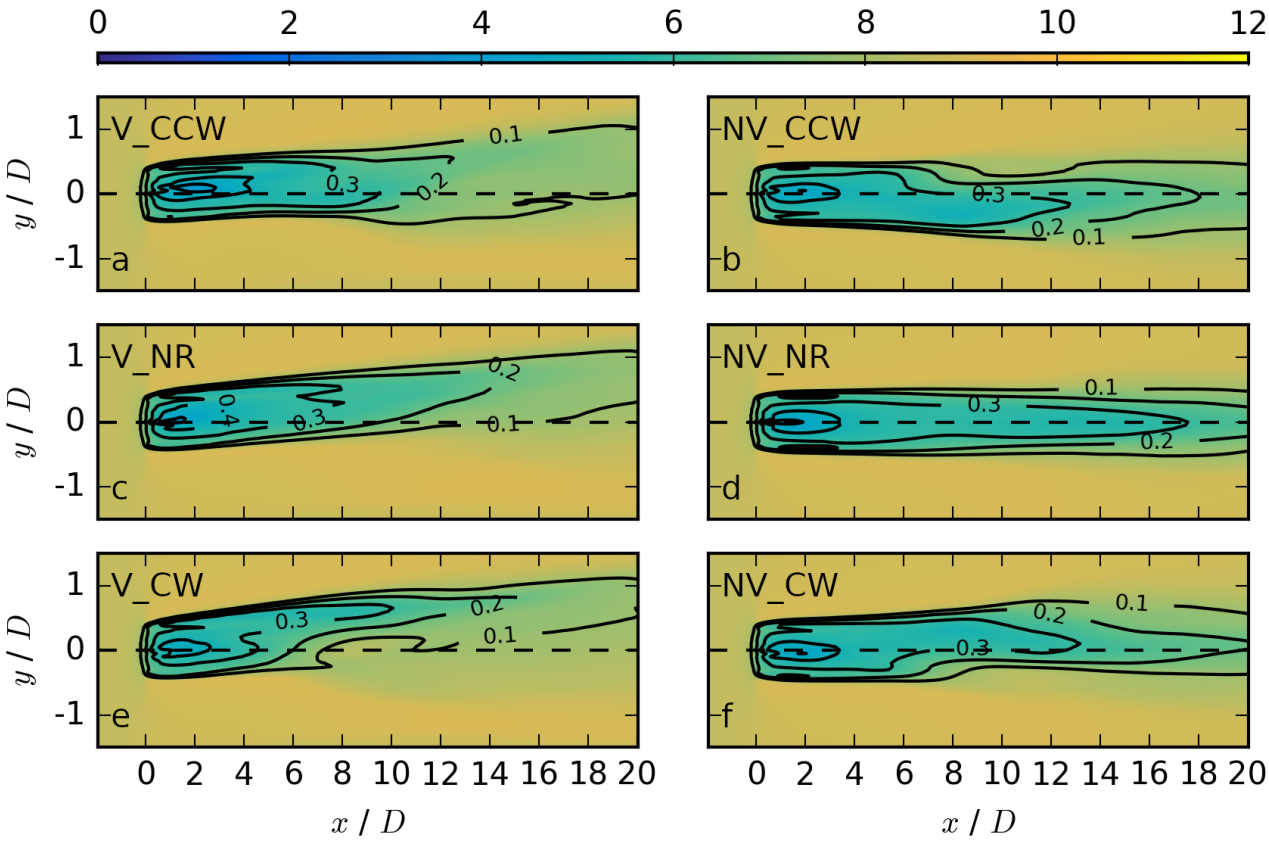

Figure 6. Coloured contours of the streamwise velocity $\overline{u_{i,j,k_*}}$ in m s^{-1} at z = 75 m with index k_*, averaged over the last 10 min, for the same cases as in Fig. 4. The black contours represent the velocity deficit VD_{i,j,k_*} at the same vertical location.

rapid wake recovery in all heights in the far wake. In comparison to the veering impact for a clockwise rotating blade, it is much larger in case of a counterclockwise rotating blade (Fig. 7(a)). This is related to the much larger difference in total turbulence intensity between V_CW and NV_CW in comparison to V_CCW and NV_CCW (Fig. 7(b)). The veering wind further impacts the wake deflection angle. The wakes in the veered simulation V_CW as well as in the non-veered simulation NV_CW are deflected towards the south (north) in the upper (lower) rotor part with a larger wake deflection angle in V_CW (Fig. 5(e), (f) (Fig. 6(e), (f))). The same northward wake deflection in the upper (Fig. 5(e), (f)) and the same southward wake deflection in the lower (Fig. 6(e), (f)) rotor part for V_CW and NV_CW result from the interaction of a counterclockwise blade rotation with veered and non-veered inflow conditions. It contrasts the changes in height in the wake deflection from northward to southward in V_CCW (Fig. 6(a) vs. Fig. 5(a)) and vice versa in NV_CCW (Fig. 6(b) vs. Fig. 5(b)). As the wake deflection angle has the same sign by comparing V_CW and NV_CW in comparison to V_CCW and NV_CCW (Figs. 5, 6), the spanwise profiles in Fig. 7(c) and (g) are positive in the rotor region with only a slightly shift of the maximum from y / D = 0. Further, the wake width

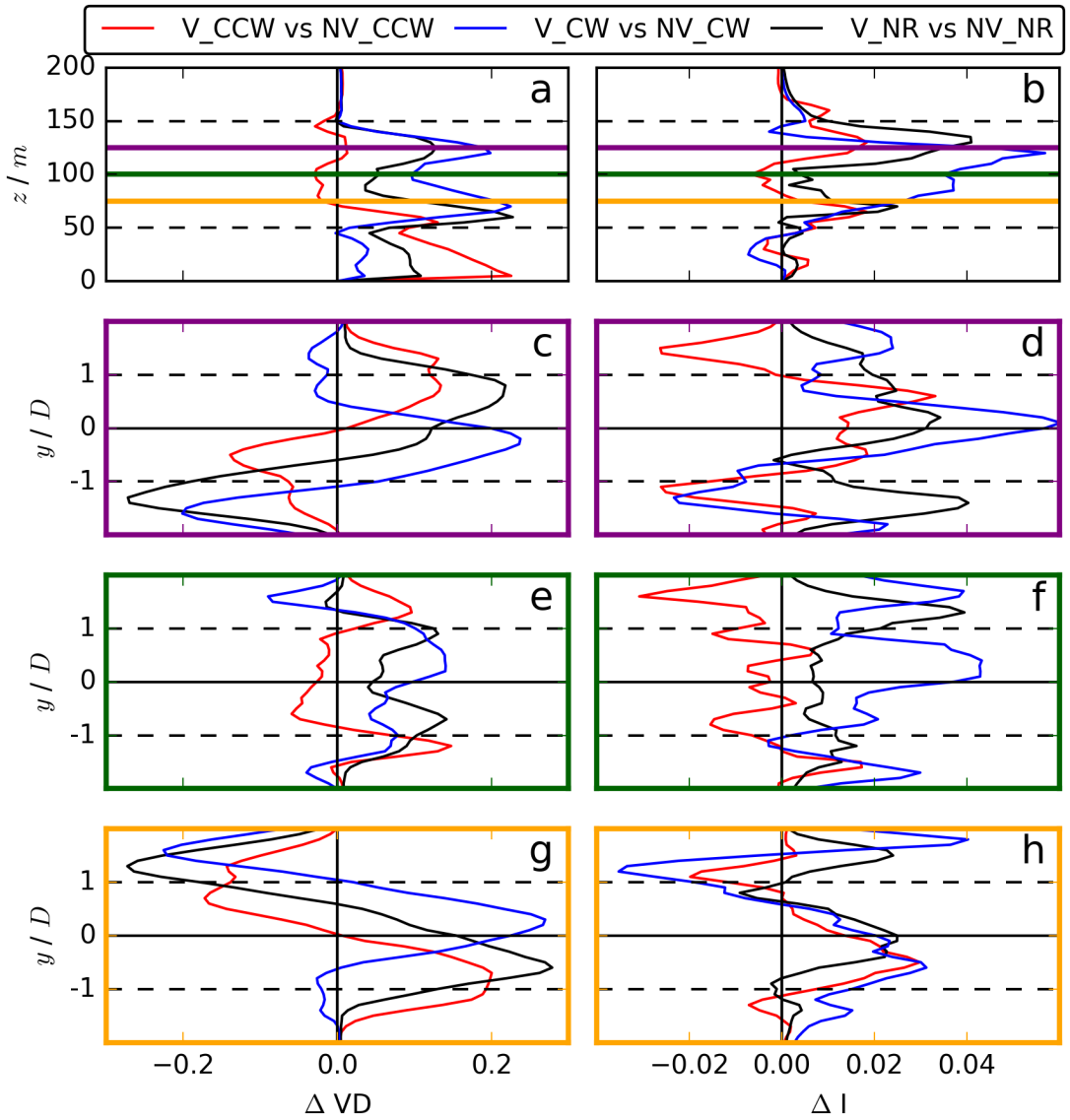

Figure 7. Vertical and spanwise profiles of ΔVD in (a), (c), (e), (g) and ΔI in (b), (d), (f), (h) at 10 D. The spanwise profiles are plotted at 75 m (orange frame, (g), (h)), 100 m (hub height) (green frame, (e), (f)), and 125 m (purple frame (c), (d)). In panels (a) and (b), the coloured lines indicate the altitudes analysed in (c) - (h). Considering a comparison of two simulations A and B (see legend: A vs B), ΔVD is calculated as the difference between simulation B and simulation A $VD(B) - VD(A)$ and ΔI as the difference between simulation A and simulation B $I(A) - I(B)$. Therefore, $\Delta VD > 0$ and likewise $\Delta I > 0$ represent a more rapid wake recovery of simulation A in comparison to simulation B, related to a higher turbulence intensity level.

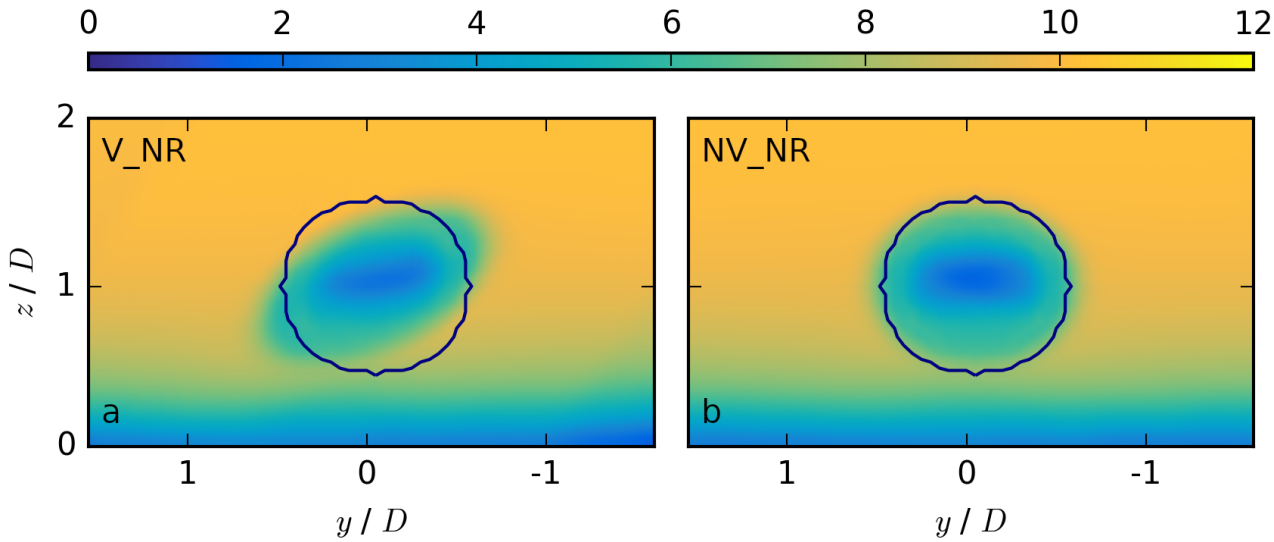

Figure 8. Coloured contours of the streamwise velocity $\overline{u_{i,j,k_h}}$ in m s^{-1} at a downward position of 5 D behind the rotor, averaged over the last 10 min, for V_NR in (a) and NV_NR in (b). The black contour represents the actuator.

in the far wake differs, especially at hub height (Figs. 4(e), (f)). As this is not the case in V_CCW vs. NV_CCW (Figs. 4(a) vs. (b)), it is also an effect of the interaction of counterclockwise rotating blades with a veering wind. In summary, the differences between the veered and the corresponding non-veered simulations are much larger for a clockwise wake rotation in comparison to a counterclockwise one.

As an intermediate step, we investigate the rotational effect under veered inflow conditions by comparing V_CCW with V_NR. The veered inflow condition in combination with clockwise rotating blades results in a more rapid flow recovery at hub height in V_CCW (Fig. 4(a)) in comparison to V_NR (Fig. 4(c)). At 10 D the wake in the center part of the rotor recovers more rapidly in case of V_CCW in comparison to V_NR (Fig. 9(e)). Defining a wake deflection angle of zero for a non-deflected wake, the combination of veered inflow conditions and clockwise disc rotation reduces the wake deflection angle in the top-tip (Fig. 5(a)) and the bottom-tip sectors (Fig. 6(a)) in V_CCW in comparison to V_NR (Figs. 5(c), 6(c)). Both effects arise from a clockwise blade rotation and are responsible for the axis-symmetric behavior of ΔVD with a more rapid wake recovery of V_CCW in one rotor half and a less rapid one in the other in Fig. 9(c) and (g).

To further investigate the impact of the rotational direction, we also compare V_CW to V_NR. Here, a more rapid wake recovery persists in the wake over the whole rotor in V_CW in comparison to V_NR (Fig. 9(a), (c), (e), (g)), which is especially pronounced at hub height (Fig. 4(e) vs. Fig. 4(c), (Fig. 9(e))), resulting from a higher turbulence level in V_CW in comparison to V_NR (Fig. 9(b), (d), (f), (h)). Further, counterclockwise rotating blades increase the wake deflection angle in the top-tip (Fig. 5(e)) and the bottom-tip sectors (Fig. 6(e)) in V_CW in comparison to V_NR (Figs. 5(c), 6(c)), and likewise especially in comparison to V_CCW (Figs. 5(a), 6(a)).

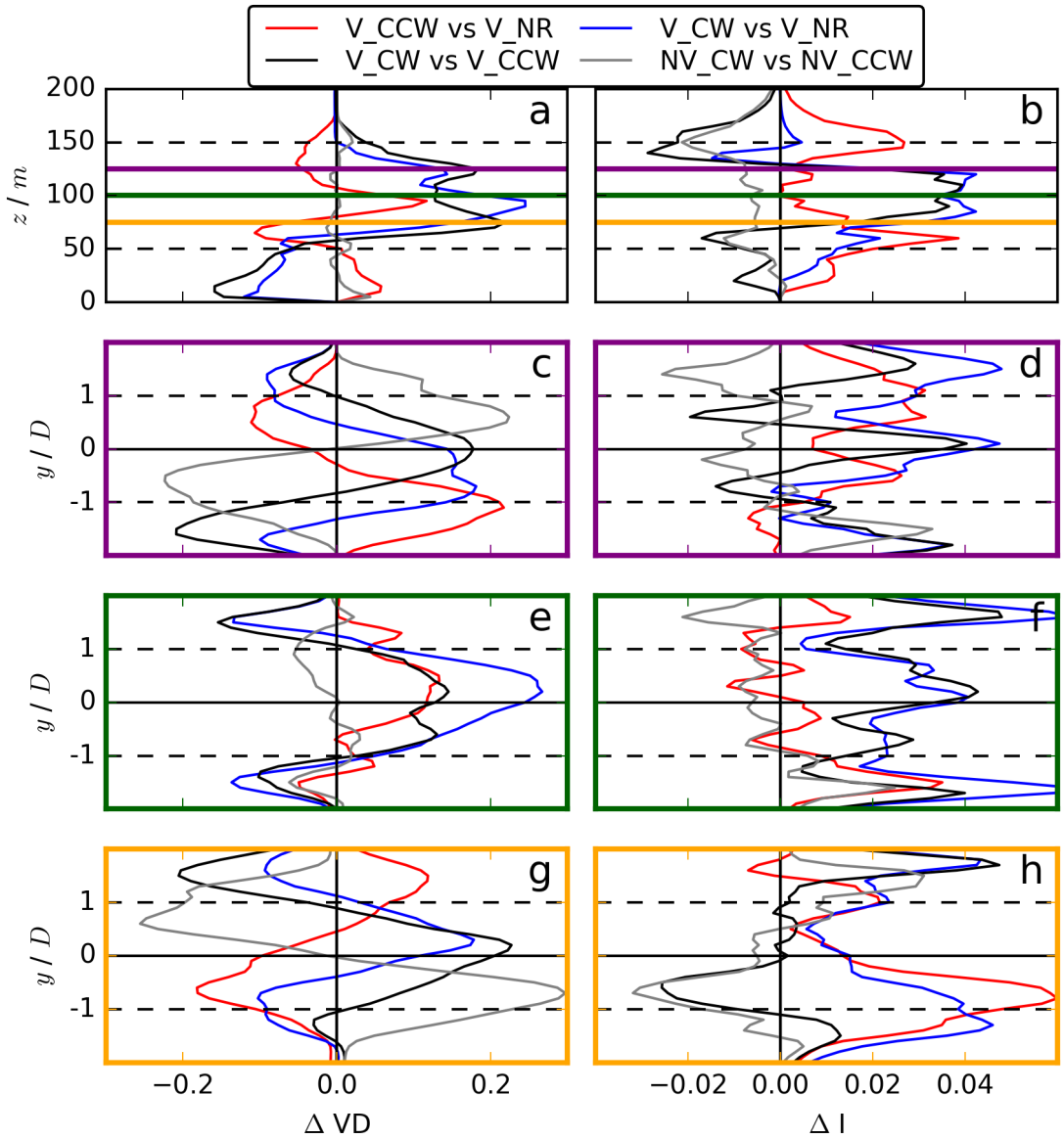

Figure 9. Vertical and spanwise profiles of ΔVD in (a), (c), (e), (g) and ΔI in (b), (d), (f), (h) at 10 D. The spanwise profiles are plotted at 75 m (orange frame, (g), (h)), 100 m (hub height) (green frame, (e), (f)), and 125 m (purple frame (c), (d)). In panels (a) and (b), the coloured lines indicate the altitudes analysed in (c) - (h). Considering a comparison of two simulations A and B (see legend: A vs B), ΔVD is calculated as the difference between simulation B and simulation A $VD(B) - VD(A)$ and ΔI as the difference between simulation A and simulation B $I(A) - I(B)$. Therefore, $\Delta VD > 0$ and likewise $\Delta I > 0$ represent a more rapid wake recovery of simulation A in comparison to simulation B, related to a higher turbulence intensity level.

Table 3. The main results of each comparison are listed regarding the streamwise elongation of the wake, the wake deflection angle and the spanwise wake width.

COMPARISON OF	elongation of wake	wake deflection angle	wake width	WITH
V_NR	$<$	$>$	$\approx$	**NV_NR**
V_CCW	$\geq$	opposite sign	$\approx$	**NV_CCW**
V_CW	$<$	$>$	$<$	**NV_CW**
V_CCW	$<$	$<$	$\approx$	**V_NR**
V_CW	$<$	$>$	$\approx$	**V_NR**
V_CW	$<$	$>$	$>$	**V_CCW**
NV_CW	$\approx$	axis-symmetric	$\approx$	**NV_CCW**

Therefore, the direct comparison of V_CW and V_CCW (Figs. 4(e) vs. (a), 5(e) vs. (a), and 6(e) vs. (a), 9) reveals that the wake recovery, the wake deflection angle, and the wake width depend on the rotational direction of the wind turbine. In V_CW, the wake recovers more rapidly over the whole rotor (Figs. 4(e) vs. (a), 9(a), (c), (e), (g)). The wake deflection angle is much larger in V_CW in comparison to V_CCW (Figs. 5(e) vs. (a), 6(e) vs. (a)). This can be interpreted as a weakening of the wake deflection angle in case of a clockwise rotating wind turbine and an amplification in case of a counterclockwise rotating one. Further, the wake width is larger in spanwise direction in V_CW in comparison to V_CCW (Figs. 4(e) vs. (a)).

In comparison, in the non-veered simulations NV_CW and NV_CCW, the impact of the rotational direction on the wake recovery is very limited in the near wake and slightly increases in the far wake at hub height (Figs. 4(b) vs. (f), 9(a), (e)). The impact on the wake deflection angle results from the rotational direction of the wake and is nearly axis-symmetric (Figs. 5(b) vs. (f) and 6(b) vs. (f), 9(a), (e)). These differences in the non-veered simulations are in agreement with Vermeer et al. (2003), Shen et al. (2007), Sanderse (2009), Kumar et al. (2013), Hu et al. (2013), Yuan et al. (2014) and Mühle et al. (2017). Comparing ΔV of NV_CW vs. NV_CCW to V_CW vs. V_CCW in Fig. 9(a), the rotational direction impact under non-veered inflow conditions is rather small approaching zero and can be considered of minor importance for a possible downwind turbine, whereas the rotational direction impact under veered conditions is much larger and significant for downwind turbines.

A summary of all main results regarding the streamwise elongation of the wake, the wake deflection angle and the wake width is given in Table 3. Considering all of these comparisons, the differences in the streamwise elongation of the wake, the spanwise wake width, and the wake deflection angle between V_CW and V_CCW are a superposition effect of wind veer and clockwise wake rotation, as they do not occur to the same extent for a counterclockwise wake rotation in combination with the same veered inflow conditions. Further, the differences do not occur at all under non-veered inflow conditions, independent of the rotational direction. The responsible mechanism behind this striking difference in the streamwise velocity and total turbulence intensity profiles for the combination of veered inflow conditions with counterclockwise rotating blades in comparison to clockwise rotating blades will be evaluated in more detail below.

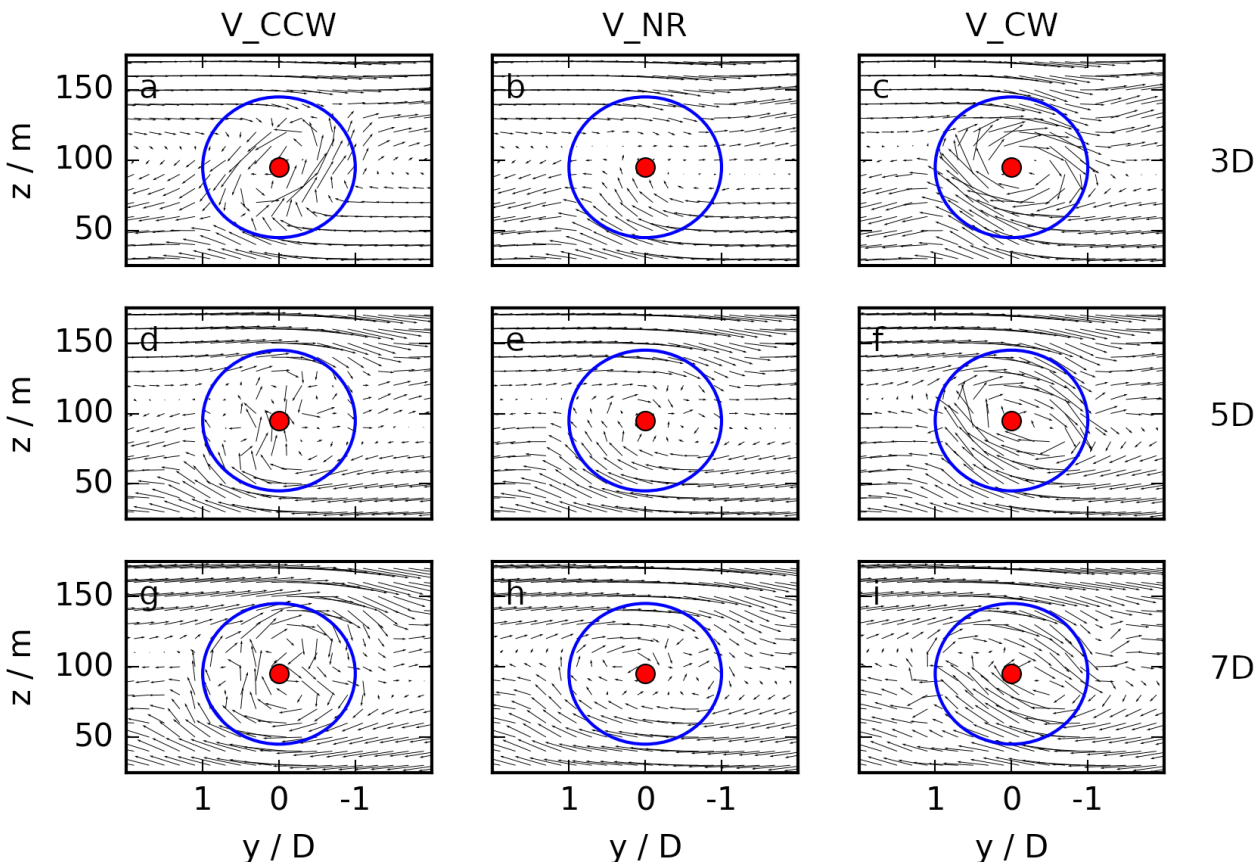

Figure 10. Flow rotation of v and w at 3D (first row), 5D (second row), and 7D (third row) behind the disc for V_CCW (left column), V_NR (middle column), and V_CW (right column). The red dot marks the rotor center and the blue contour the rotor region.

3.2 Impact on Spanwise and Vertical Velocity Components

The combination of a veering wind with both rotational directions of the rotor not only impact the streamwise velocity and the total turbulence intensity, they also have an influence on the spanwise v and vertical wind w components. Figure 10 represents the flow fields of v and w at 3 D, 5 D and 7 D for the three veered cases. At 3 D, the flow field in the rotor region of V_NR (Fig. 10(b)) is only determined by the boundary-layer flow which is decelerated due to its interaction with the rotor. The flow field in the rotor region in V_CW (Fig. 10(c)) shows the same rotational direction as the wake flow and V_NR. The interaction of both flow fields results in an intensified rotation in the rotor region. V_CCW shows the opposite rotational direction of the flow field in the rotor region in comparison to V_NR and V_CW (Fig. 10(a)). The interaction weakens the rotor-induced rotation in the rotor region. The vorticity in the rotor region is therefore weaker in V_CCW in comparison to V_CW (Fig. 10(a) vs. (c)). At 5 D, the rotational direction in V_CW is the same as at 3 D (Fig. 10(f) vs. (c)), with a comparable strength of the v

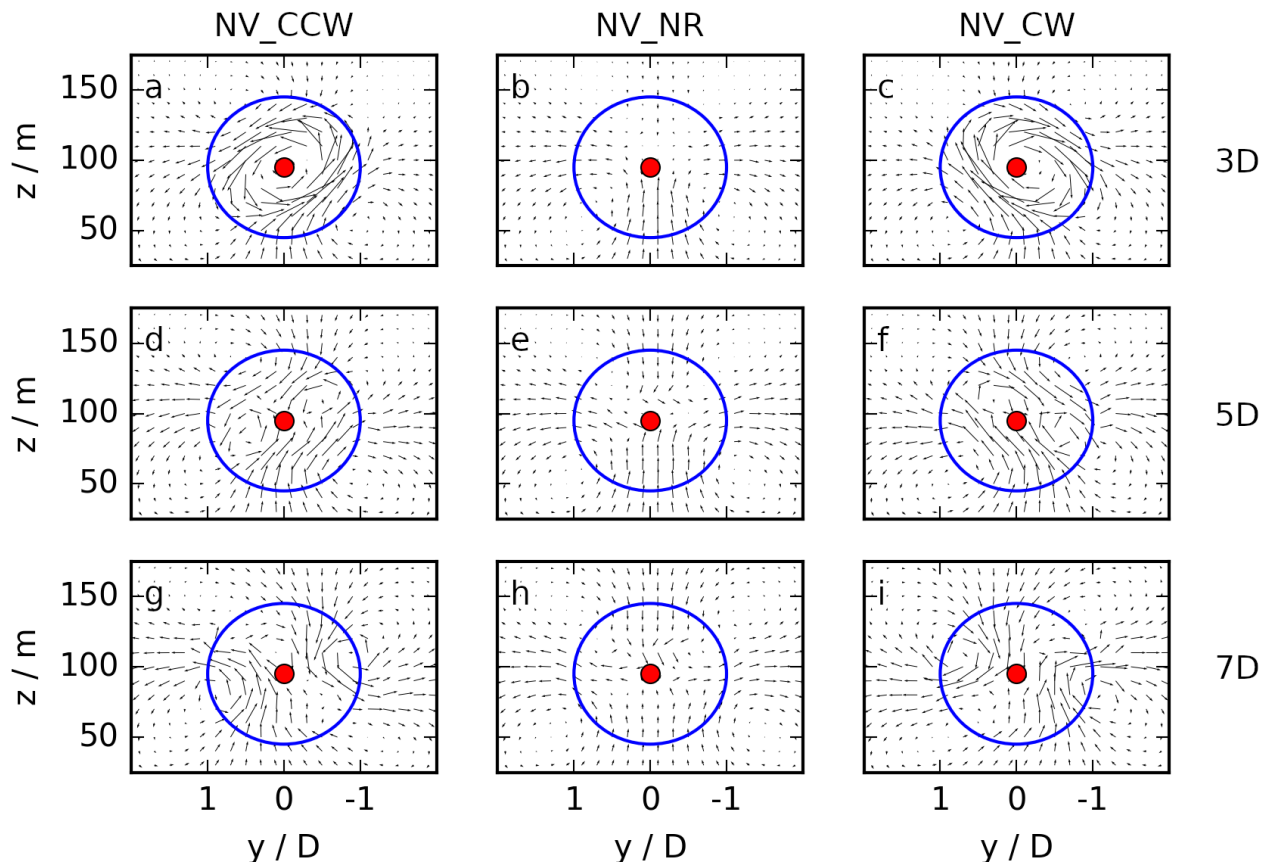

Figure 11. Flow rotation of v and w at 3D (first row), 5D (second row), and 7D (third row) behind the disc for NV_CCW (left column), NV_NR (middle column), and NV_CW (right column). The red dot marks the rotor center and the blue contour the rotor region.

and w flow fields and likewise of the rotational direction. In V_CCW, however, the rotation of the flow field induced by the rotor disappears and the boundary-layer flow field now dominates (Fig. 10(d) vs. (a)). At 7 D, the flow rotation in the rotor region is the same in V_CCW and V_CW, with a much more pronounced rotation pattern in V_CW (Fig. 10(g) vs. (i)). In V_CCW, the wind turning of the Ekman spiral emerges in the rotor region at 7 D (Fig. 10(g)), an effect related to the overlapping of the veering wind in the boundary-layer flow with an opposite directed flow rotation induced by the rotor.

The non-veered cases are presented in Fig. 11. The differences surrounding the rotor in NR between NV_ (Fig. 11) and V_ (Fig. 10) result from the ABL flow field and can be related to the differences in the inflow conditions in Fig. 2. In detail, at 3 D, the flow field in the rotor region of NV_NR (Fig. 11(b)) is again only determined by the boundary-layer flow, with $v_{BL}(z) = 0$ and $w_{BL}(z) = 0$, and the deceleration due to the interaction with the rotor. The arising pattern is related to the flow deceleration of the non-rotating disc. NV_CCW (Fig. 11(a)) and NV_CW (Fig. 11(c)) are axis-symmetric to each other. Here the vorticity is comparable in both simulations, as it is only determined by the tangential force imposed by the wind-turbine

parametrization $\mathbf{F}_\Theta$ in Eq. 1. The opposite rotational direction is related to the opposite sign of β_v and β_w. The axis-symmetric structure persists up to 7 D downstream (Fig. 11(d), (g) vs. (f), (i)).

4 Simplified Wake Model

The streamwise recovery of the wake, the spanwise wake width, and the wake deflection angle differ between V_CCW and V_CW, while these differences do not emerge in the non-veered cases NV_CCW and NV_CW. The flow fields of v and w differ between V_CCW and V_CW, whereas v and w are axissymmetric in NV_CCW and NV_CW. The different behavior of V_CW in comparison to V_CCW arises from the interaction of the Ekman spiral in the boundary-layer flow with the clockwise flow rotation induced by the counterclockwise rotating rotor.

4.1 Model Development

To demonstrate this interaction and the difference between V_CW and V_CCW, we introduce a simplified wake model, which is a linear superposition of the atmospheric boundary-layer flow u_{BL}, v_{BL}, and w_{BL} (Equations 4, 5, and 7) with a wind-turbine model. The wind-turbine model includes the axial turbine-induced force $\mathbf{F}_x$, as well as the tangential turbine-induced force $\mathbf{F}_\Theta$, which correspond to a Rankine Vortex (RV) (Lamb, 1993)

$$u_{WT} = 0.3 \cdot u_{BL} \tag{13}$$

$$v_{WT} = v_{RV} = \pm \omega r \frac{r}{R} cos(\Theta) \tag{14}$$

$$w_{WT} = w_{RV} = \mp \omega r \frac{r}{R} sin(\Theta), \tag{15}$$

with ω representing the angular velocity of the flow induced by the angular velocity of the wind turbine Ω, r, and Θ correspond to the position in the disc region and R to the rotor radius. Equation 13 is motivated by Fig. 4. Here, the flow is not completely decelerated directly behind the disc, $u(rotor) > 0$, as in EULAG the rotor of a wind turbine is not implemented as a real circular obstacle (e.g. grid-point blocking as in Heimann et al. (2011)). Instead, at every grid point covered by the rotor, the streamwise velocity field experiences the turbine-induced force $\mathbf{F}_x$ according to Eq. 1. This implementation is inspired by the immersed boundary method (Smolarkiewicz and Winter, 2010). Considering this, the wind-turbine model includes a certain fraction of u_{BL} in u_{WT}. We apply a fraction of 0.3, which can be related to $VD_{max} = 0.7$ of the rotating disc simulations in Fig. 4 and consequently to an axial induction factor a of 0.7, resulting in a fraction of 0.3 = (1-a), as it would be the case by calculating the axial force with momentum theory (Manwell et al., 2002; Hansen, 2008).

The simplified wake model (M) results from a linear superposition of the boundary layer flow with the wind-turbine induced forces on the flow field:

$$u_M = u_{BL} - u_{WT} \tag{16}$$

$$v_M = v_{BL} \pm v_{WT} \tag{17}$$

$$w_M = \pm w_{WT} \tag{18}$$

and inserting Equations 4, 5, and 7 and Equations 14 and 15, a wake model arises, which depends on the radial position of the wake r.

$$u_M(r) = u_g \cdot \left(1 - exp\left(-\frac{z\sqrt{f/\kappa}}{\sqrt{2}}\right)\right) - 0.3 \cdot u_g \cdot \left(1 - exp\left(-\frac{z\sqrt{f/\kappa}}{\sqrt{2}}\right)\right) \tag{19}$$

$$v_M(r) = tan\left(\left(270^\circ - \left(262^\circ + 8^\circ \frac{z}{100m}\right)\right)\frac{\pi}{180^\circ}\right) \cdot u_g \cdot \left(1 - exp\left(-\frac{z\sqrt{f/\kappa}}{\sqrt{2}}\right)\right) \pm (\pm\omega r \frac{r}{R} cos(\Theta)) \tag{20}$$

$$w_M(r) = \pm(\mp\omega r \frac{r}{R} sin(\Theta)) \tag{21}$$

For completing a more realistic wake model, two effects need to be considered:

1. The position of the complete wake recovery x_{rec} with $u(x_{rec}) = u_{BL}$ in relation to each downstream position x_{pos} ($x_{rec} > 20$ D according to Figures 4, 5, and 6).

2. The downstream erosion of v_{WT} and w_{WT} with x_{fad} corresponding to a prescribed decay distance at which the atmospheric boundary-layer flow determines the rotational direction of the wake (3 D $< x_{fad} <$ 5 D according to Figure 10).

In Equations 22, 23, and 24, we present the modification of Eqs. 19 - 21 leading to a simplified wake model, which depends both on the radial position of the wake r and on the downwind position x_{pos}:

$$u_M(r, x_{pos}) = u_{BL} - 0.3 \cdot u_{BL}\left(\frac{x_{rec} - x_{pos}}{x_{rec}}\right) \tag{22}$$

$$v_M(r, x_{pos}) = \left(v_{BL} \pm (\pm\omega r \frac{r}{R} cos(\Theta))\left(\frac{1}{exp\frac{x_{pos}}{x_{fad}}}\right)^\delta\right)\left(\frac{x_{pos}}{x_{rec}}\right)^\gamma \tag{23}$$

$$w_M(r, x_{pos}) = \pm(\mp\omega r \frac{r}{R} sin(\Theta)) \cdot \left(\frac{1}{exp\frac{x_{pos}}{x_{fad}}}\right)^\delta \cdot \left(\frac{x_{pos}}{x_{rec}}\right)^\gamma, \tag{24}$$

with δ describing the attenuation of the rotor-induced rotation with distance and γ the wake recovery due to the entrainment of ambient boundary-layer air.

4.2 Comparison with Simulation Results

This simplified model is able to capture the simulated behavior of the LESs. Figure 12 compares the results of the veered simulations V_CCW and V_CW to this simplified wake model (Equations 22 - 24). The left panel shows the sector averaged velocity values of u and v of the top-tip and the bottom-tip sectors. The velocity values of w correspond to the right and the left sectors, also for both rotational directions. In the simplified wake model, we apply the parameters $z = 145$ m and $\Theta = 0\,^\circ$ for the top-tip sector, and $z = 55$ m and $\Theta = 180\,^\circ$ for the bottom-tip sector as well as $\Theta = 90\,^\circ$ for the right sector and $\Theta = 270\,^\circ$ for the left sector. Further, $u_g = 10$ m s^{-1}, $\omega = 7$ rpm, $x_{rec} = 25$ D, $x_{fad} = 4$ D, γ=0.4, and δ=2.5. The values of γ and δ are determined by empirical fitting.

The main characteristics are very well represented by the simplified wake model, especially for the $\overline{v}$ and $\overline{w}$ components. It can reproduce the change of the flow rotation in the wake in CCW and the correct signs of $\overline{v}$ and $\overline{w}$ for both rotational directions.

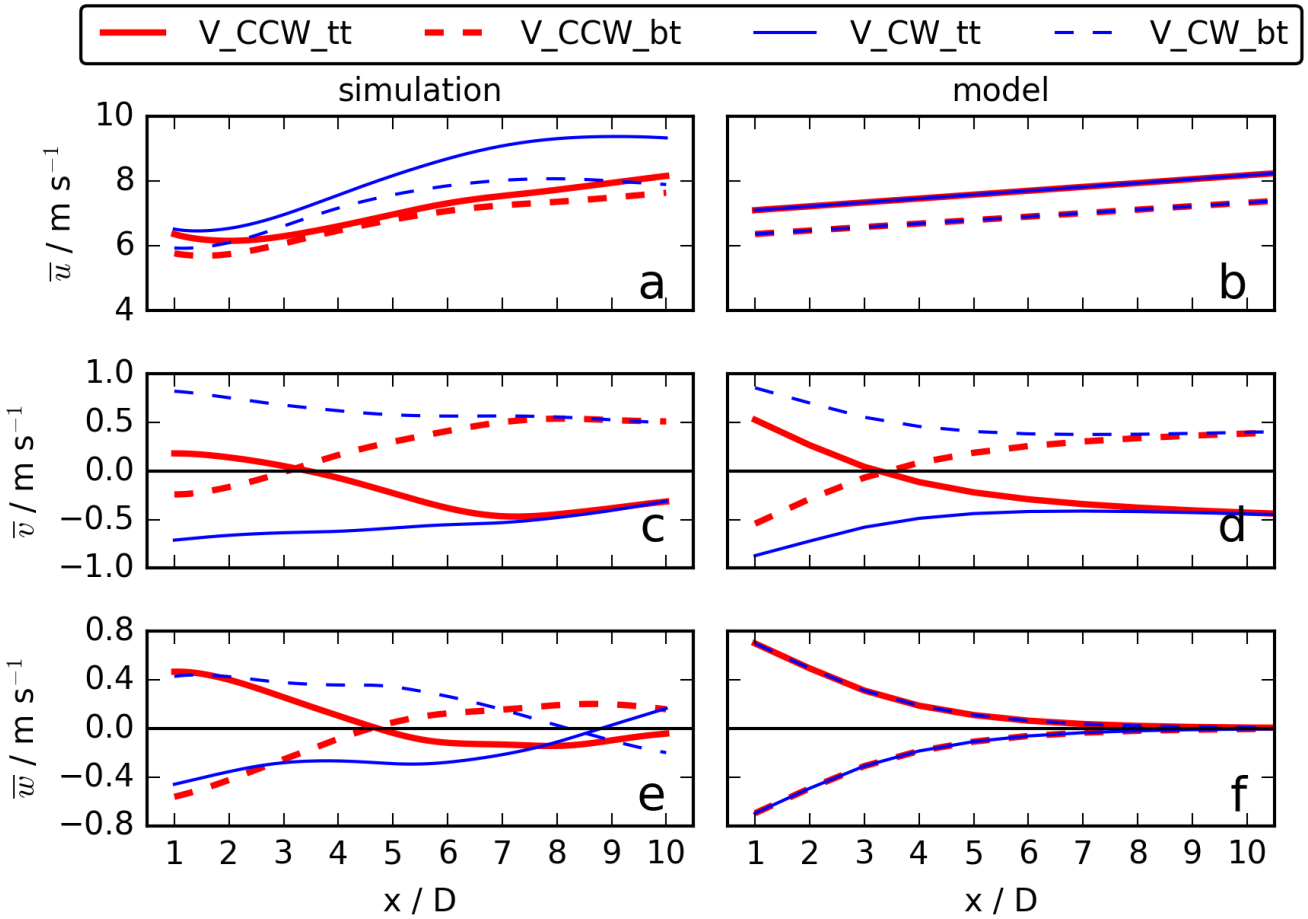

Figure 12. Sector averages of $\overline{u}$ in (a), $\overline{v}$ in (c), and $\overline{w}$ in (e) according to Fig. 3 for the veered cases V_CCW and V_CW. $\overline{u}$ and $\overline{v}$ show the top-tip and bottom-tip sectors, $\overline{w}$ the right (solid line) and left (dashed line) sectors. The corresponding model components are shown in (b) for $\overline{u}$, (d) for $\overline{v}$, and (f) for $\overline{w}$.

In more detail, the simulation results in Fig. 12(a) show a larger zonal wind in the top-tip sector, which is directly related to $u_{BL}(tt) > u_{BL}(bt)$ in Eq. 4. This effect is represented by the simplified wake model in Fig. 12(b). Further, the $\overline{u}$-values are larger in V_CW in comparison to V_CCW. This results from the interaction of u with v and w. The simplified wake model did not consider this interaction, leading to an overlap of both top-tip and bottom-tip sectors in Fig. 12(b). Further, in the simplified wake model, the zonal wind values are smaller in comparison to the simulation results. In addition to a different choice of the prefactor of 0.3 in u_{WT}, this magnitude can also be modified by the wake recovery parameter γ, where a smaller value results in larger zonal wind values.

The simulation behavior of the meridional wind $\overline{v}$ in Fig. 12(c) differs depending on the rotational direction of the wake (CCW or CW). First, the opposite sign of $\overline{v}$-values prevails in both top-tip (bottom-tip) sectors in the near wake (as it is the

case in the non-veered simulations (not shown here)). Second, an additional change of the sign in $\overline{v}$ occurs only in CCW between 3 D and 4 D, a downstream position which is similar to x_{fad} in Fig. 10. The sign does not dominate if wind veer interacts with a clockwise rotating wake (CW). This interaction in the CCW-case can be explained with the simplified wake model by a linear superposition of v_{BL} with v_{WT}. The downstream position of the change of the sign in v in the simplified wake model for the counterclockwise case can be modified with the entrainment parameter δ, whereas a larger δ-value results in a smaller downstream distance of the crossover as the impact of the boundary-layer flow on the wake sets in closer to the rotor. Further, the magnitude of $v_M(r, x_{pos})$ agrees with the simulation results. This agreement is the reason why we did not choose a smaller γ-value to increase $u_M(r, x_{pos})$, as it would likewise increase the magnitude of $v_M(r, x_{pos})$. Third, the magnitude of the $\overline{v}$-values is much smaller in the near wake in CCW in comparison to CW. In the far wake at $x > 7$ D, the magnitude of $\overline{v}$ is the same in both cases CCW and CW, as the rotational direction impact is marginal and the flow field is only determined by the Ekman spiral. The smaller $\overline{v}$-values in CCW result from the overlapping of a counterclockwise wake rotation with the Ekman spiral in the rotor region (Fig. 10(a)), whereas the overlapping of a clockwise rotating wake with the same Ekman spiral increases the $\overline{v}$-values in the near wake rotor region (Fig. 10(c)), both in comparison to $x > 7$ D.

The simulation behavior of the vertical component $\overline{w}$ in the right and left sectors in Fig.12(e) is determined by the downward transport of higher momentum air from above or the upward transport of lower momentum air from below. In V_CCW (V_CW), higher momentum air is transported downwards from the top-tip sector into the right (left) sector, resulting in negative vertical velocity values in the right (left) sector. In CCW, the crossing of zero between 4 D and 5 D corresponds to the difference between 3 D and 5 D in the left and right sectors and to x_{fad} (Fig. 10). By changing the rotational direction, the positive and negative components change in both sectors. The crossing of zero occurs further downstream in CW due to the intensification of the boundary-layer flow and the rotational direction induced on the flow by the rotor. The general behavior of positive and negative values can be represented with the simplified wake model in Fig. 12(f). As the only difference in the vertical component of the simplified wake model is the sign of w_{WT}, the curves for both rotational directions overlap. However, the crossing of zero is not represented, as this effect is not only a linear superposition effect.

Further, the main patterns of the simplified wake model for the non-veered case also agree with the simulation results of NV_CCW and NV_CW. The results are not shown in the scope of this work, however, they are straightforward with the only difference of $v_{BL} = 0$ in Eq. 23.

5 Impact of Rotational Direction on the Flow in the Wake

The simplified wake model was introduced to explain the interaction between the incoming veering wind and opposite rotational directions by a linear superposition of both flow fields. The other essential ingredient is the attenuation of rotation and wake recovery by entrainment downstream of the rotor. The difference between the flow structure in the wake of simulation pairs V_CCW and V_CW and likewise the absence of this difference in NV_CCW and NV_CW could be explained by this simple model.

The resulting flow structures in the wakes are sketched and summarized in Fig. 1. In the cases without wind veer but with blade rotation, NV_CCW and NV_CW (Fig. 1(b), (f)), the rotational direction of the flow impressed by the corresponding blade rotation persists through the whole wake with decreasing strength as the wake evolves downwind. In the case of no blade rotation and no wind veer (NV_NR, Fig. 1(d)), no rotation of the flow occurs in the wake.

If a stably stratified ABL with a veering wind, described by an Ekman spiral characteristic of the Northern Hemisphere, interIf a stably stratified ABL with a veering wind, described by an Ekman spiral characteristic of the Northern Hemisphere, interacts with clockwise rotating blades (V_CCW), the rotational direction of the flow in the near wake is opposite from the far wake (Fig. 1(a)). In the near wake, the counterclockwise rotating flow results from clockwise rotating blades, whereas the strength of flow rotation mainly depends on ω (Eqs. 14 and 15). This impact on the wake decreases with further distance downwind. In the far wake, wake rotation becomes smaller than the rotational direction component imposed on the flow by the veering wind. At that point, the rotational direction of the wake is determined by the ABL flow and its veering wind as it is the case in the whole wake if a stably stratified ABL with wind veer interacts with a non-rotating actuator. The change of the rotational direction of the flow in the wake in V_CCW (Fig. 1(a)) explains the different behavior of flow recovery in the near wake and the far wake between V_CCW (Fig. 4(a)) and V_NR (Fig. 4(c)) and is also responsible for the smaller wake deflection angle in V_CCW in comparison to V_NR (Fig. 5(a) vs. (c) and Fig. 6(a) vs. (c)).

Considering the same stably stratified ABL with a veering wind, where the same Ekman spiral interacts with counterclockwise rotating blades (V_CW), the flow in the near wake consequently rotates in a clockwise direction (Fig. 1(e)). This rotational direction of the flow persists in the whole wake, as the rotational direction imposed by the ABL also results in a clockwise flow rotation in the far wake, where it becomes larger than the rotational direction component imposed on the flow by blade rotation. The resulting different rotational directions of the flow in the near wake in V_CW and V_CCW (Fig. 1(e) vs. (a)) explain the differences in the flow recovery (Fig. 4(e) vs. (a)), in the spanwise wake width (Fig. 4(e) vs. (a)), and in the wake deflection angle (Fig. 5(e) vs. (a) and Fig. 6(e) vs. (a)).

Consequently, the rotational direction of the flow in the near wake is determined by the rotational direction of the wind turbine, whereas the rotational direction of the flow in the far wake is determined by the ambient wind veer, often dictated by the direction of the Ekman spiral and thus by the sign of the Coriolis force and the hemisphere. If the rotational directions of the flow in the near wake and the boundary-layer flow intensify each other, the same rotational direction persists in the whole wake, as it is the case for a counterclockwise rotating wind turbine (V_CW). Otherwise, the rotational direction of the flow will change in the wake as for a clockwise rotating wind turbine under veered inflow conditions at night in the Northern Hemisphere (V_CCW). The position of the change of rotational direction, x_{fad}, depends on the strength of rotational direction imposed by the blades (Ω) and likewise on the strength of the veering wind, with a smaller rotational speed or a larger wind veer resulting in a smaller x_{fad}.

6 Conclusions

To investigate the interaction of a veering wind with the rotational direction of a wind turbine in the wake in a stably stratified ABL, we carry out a series of six LESs varying the incoming wind condition and both the magnitude and direction of the wind turbine rotation.

The rotational direction of a wind turbine rotor in a stably stratified ABL without wind veer only exerts a minor influence on the wake behavior. This minor impact is consistent with previous investigations by Vermeer et al. (2003), Shen et al. (2007), Sanderse (2009), Kumar et al. (2013), Hu et al. (2013), Yuan et al. (2014), and Mühle et al. (2017).

In the presence of wind veer, the rotational direction of a wind turbine, however, clearly impacts the streamwise elongation of the wake, the spanwise wake width, and the wake deflection angle. The resulting flow structures in the wake answer the posed question with a clear yes, the rotational direction of a wind turbine impacts the wake in a stably stratified ABL. The LESs are controlled by the rotational direction of the wind-turbine wake imposed by the blades (clockwise (CW) vs. counterclockwise (CCW) vs. no rotation (NR)) and the inflow wind profiles (wind veer (V) vs. no wind veer (NV)). In detail, in case of a non-rotating actuator, the rotation of the flow in the wake is only determined by the SBL regime. If the rotational direction of the wake and the SBL are the same, also one rotational direction persists in the whole wake, as it would be the case for counterclockwise rotating blades in the Northern Hemisphere (V_CW). In case of the common clockwise rotating blades (V_CCW), the rotational direction in the near wake, imposed by the rotor, differs from the rotational direction in the far wake, induced by the veering wind in the stably stratified regime in the Northern Hemisphere.

Wind veer occurs in a stably stratified ABL as long as the flow is not channeled. Veer reflects the change of Coriolis force and friction with height in the absence of convective buoyancy, and therefore happens on many nights both onshore (Walter et al., 2009; Rhodes and Lundquist, 2013) and offshore (Bodini et al., 2019). According to two years of meteorological tower measurements in Lubbock (Texas) (Walter et al., 2009), a stably stratified ABL occurs in 52% of the measurements. A wind veer of 0.08 $^\circ$ m^{-1}, as applied in this paper, corresponds to a frequency of occurrence of ≈50% of the measured veering wind situations. Therefore, considering a wind turbine operating at Lubbock (Texas) would spend half of its nighttime experience under veering wind conditions similar to this study. Given the significant impact, the choice of rotational direction of wind-turbine blades in the Northern Hemisphere becomes critical.

The impact of the rotational direction of a wind-turbine rotor on the wake characteristics can be explained by the linear superposition of rotor-induced vorticity with the veering wind. A simplified wake model of a wind turbine including a Rankine Vortex and the vertically sheared and veered boundary-layer flow can explain major features of this interaction. If the main parameters (wind speed, amount of veer over the rotor, rotational frequency of the wind turbine), necessary for the simplified wake model, are known for a specific wind-turbine site, this simple model could give instantaneously a first impression about the flow fields of v and w in the wake. It could further represent the effect of a co-rotating wind turbine on its wake and, consequently, on the flow field encountered by a downwind turbine. As the operating characteristics of upwind turbines, like their yaw with incoming flow, are already being adjusted to mitigate downwind impacts of wakes (Fleming et al., 2019), this work suggests that considering the direction of rotation could have benefits as well.

These simulations represent a canonical case, and so real-world conditions may modify results. The veering wind simulated here is characteristic of a cloud free, nocturnal boundary-layer flow in the Northern Hemisphere. As the Coriolis force and the resulting Ekman spiral reverse direction in the Southern Hemisphere, the same effect should be prevalent in the Southern Hemisphere, however, with a change of wake rotation at x_{fad} for counterclockwise rotating blades instead of clockwise rotating ones as it is the case in the Northern Hemisphere. Further, canonical Ekman spirals do not occur in every stably stratified ABL conditions like cold air advection lead to a backing wind (Holton, 1973; Wallace and Hobbs, 2006), which is a wind that rotates in the counterclockwise direction with increasing height in the Northern Hemisphere. A backing wind on the Northern Hemisphere interacting with both rotational directions will result in a different impact on the wake in comparison to a veering wind on the Northern Hemisphere, and should be comparable to the Southern Hemispheric situation described above. Further, the evolution of the boundary layer through the evening transition will lead to veer profiles other than the linear profile shown here (Rhodes and Lundquist, 2013; Lee and Lundquist, 2017; Englberger and Dörnbrack, 2018a). But given the widespread occurrence of veer as noted by observational campaigns (Walter et al., 2009; Bodini et al., 2019; Sanchez Gomez and Lundquist, 2019b), as well as the interest in modifying wakes via active control of upwind turbines (Fleming et al., 2019), the work presented here can motivate further consideration of how inflow veer interacts with wind-turbine operations to affect downwind turbines.

Author contributions. All authors designed the idea. A. Englberger performed the simulations and prepared the manuscript with contributions from both co-authors.

Competing interests. The authors declare that they have no conflict of interest.

Acknowledgements. The authors gratefully acknowledge the Gauss Centre for Supercomputing e.V. (www.gauss-centre.eu) for funding this project by providing computing time on the GCS Supercomputer SuperMUC at Leibniz Supercomputing Centre (LRZ, www.lrz.de).

References

Abkar, M. and Porté-Agel, F.: The effect of atmospheric stability on wind-turbine wakes: A large-eddy simulation study, in: Journal of Physics: Conference Series, vol. 524, p. 012138, IOP Publishing, https://doi.org/10.1088/1742-6596/524/1/012138, 2014.

Abkar, M. and Porté-Agel, F.: Influence of the Coriolis force on the structure and evolution of wind turbine wakes, Physical Review Fluids, 1, 063 701, https://doi.org/10.1103/PhysRevFluids.1.063701, 2016.

Abkar, M., Sharifi, A., and Porté-Agel, F.: Wake flow in a wind farm during a diurnal cycle, Journal of Turbulence, 17, 420–441, https://doi.org/10.1080/14685248.2015.1127379, 2016.

Aitken, M. L., Kosović, B., Mirocha, J. D., and Lundquist, J. K.: Large eddy simulation of wind turbine wake dynamics in the stable boundary layer using the Weather Research and Forecasting Model, J Renew Sust Energy, 6, 1529–1539, https://doi.org/10.1063/1.4885111, 2014.

Bak, C., Zahle, F., Bitsche, R., Kim, T., Yde, A., Henriksen, L. C., Hansen, M. H., Blasques, J. P. A. A., Gaunaa, M., and Natarajan, A.: The DTU 10-MW reference wind turbine, in: Danish Wind Power Research 2013, 2013.

Bhaganagar, K. and Debnath, M.: Implications of Stably Stratified Atmospheric Boundary Layer Turbulence on the Near-Wake Structure of Wind Turbines, Energies, 7, 5740–5763, https://doi.org/10.3390/en7095740, 2014.

Bhaganagar, K. and Debnath, M.: The effects of mean atmospheric forcings of the stable atmospheric boundary layer on wind turbine wake, Journal of Renewable and Sustainable Energy, 7, 013 124, https://doi.org/10.1063/1.4907687, 2015.

Bodini, N., Zardi, D., and Lundquist, J. K.: Three-dimensional structure of wind turbine wakes as measured by scanning lidar, Atmospheric Measurement Techniques, 10, 2017.

Bodini, N., Lundquist, J. K., and Kirincich, A.: US East Coast Lidar Measurements Show Offshore Wind Turbines Will Encounter Very Low Atmospheric Turbulence, Geophysical Research Letters, 46, 5582–5591, https://doi.org/10.1029/2019GL082636, 2019.

Brugger, P., Fuertes, F. C., Vahidzadeh, M., Markfort, C. D., and Porté-Agel, F.: Characterization of Wind Turbine Wakes with Nacelle-Mounted Doppler LiDARs and Model Validation in the Presence of Wind Veer, Remote Sensing, 11, 2247, 2019.

Dörenkämper, M., Witha, B., Steinfeld, G., Heinemann, D., and Kühn, M.: The impact of stable atmospheric boundary layers on wind-turbine wakes within offshore wind farms, Journal of Wind Engineering and Industrial Aerodynamics, 144, 146–153, https://doi.org/10.1016/j.jweia.2014.12.011, 2015.

Englberger, A. and Dörnbrack, A.: Impact of Neutral Boundary-Layer Turbulence on Wind-Turbine Wakes: A Numerical Modelling Study, Boundary-Layer Meteorology, 162, 427–449, https://doi.org/10.1007/s10546-016-0208-z, 2017.

Englberger, A. and Dörnbrack, A.: Impact of the diurnal cycle of the atmospheric boundary layer on wind-turbine wakes: a numerical modelling study, Boundary-layer meteorology, 166, 423–448, https://doi.org/10.1007/s10546-017-0309-3, 2018a.

Englberger, A. and Dörnbrack, A.: A Numerically Efficient Parametrization of Turbulent Wind-Turbine Flows for Different Thermal Stratifications, Boundary-layer meteorology, 169, 505–536, https://doi.org/10.1007/s10546-018-0377-z, 2018b.

Fleming, P., King, J., Dykes, K., Simley, E., Roadman, J., Scholbrock, A., Murphy, P., Lundquist, J. K., Moriarty, P., Fleming, K., et al.: Initial results from a field campaign of wake steering applied at a commercial wind farm–Part 1, Wind Energy Science, 4, 273–285, https://doi.org/10.5194/wes-4-273-2019, 2019.

Fröhlich, J.: Large Eddy Simulation turbulenter Strömungen, Teubner Verlag / GWV Fachverlage GmbH, Wiesbaden, 414 pp, 2006.

Hansen, M. O.: Aerodynamics of wind turbines, vol. 2, Earthscan, London and Sterling, UK and USA, 181 pp, 2008.

Heimann, D., Käsler, Y., and Gross, G.: The wake of a wind turbine and its influence on sound propagation, Meteorol Z, 20, 449–460, https://doi.org/10.1127/0941-2948/2011/0273, 2011.

Holton, J. R.: An introduction to dynamic meteorology, American Journal of Physics, 41, 752–754, 1973.

Hu, H., Yuan, W., Ozbay, A., and Tian, W.: An experimental investigation on the effects of turbine rotation directions on the wake interference of wind turbines, in: 51st AIAA Aerospace Sciences Meeting including the New Horizons Forum and Aerospace Exposition, p. 607, 2013.

Kühnlein, C., Smolarkiewicz, P. K., and Dörnbrack, A.: Modelling atmospheric flows with adaptive moving meshes, J Comput Phys, 231, 2741–2763, https://doi.org/10.1016/j.jcp.2011.12.012, 2012.

Kumar, P. S., Abraham, A., Bensingh, R. J., and Ilangovan, S.: Computational and experimental analysis of a counter-rotating wind turbine system, 2013.

Lamb, H.: Hydrodynamics, Cambridge university press, 1993.

Lee, J. C. and Lundquist, J. K.: Observing and Simulating Wind-Turbine Wakes During the Evening Transition, Boundary-Layer Meteorology, 164, 449–474, https://doi.org/10.1007/s10546-017-0257-y, 2017.

Manwell, J., McGowan, J., and Roger, A.: Wind Energy Explained: Theory, Design and Application, Wiley: New York, NY, USA, 134 pp, 2002.

Margolin, L. G., Smolarkiewicz, P. K., and Sorbjan, Z.: Large-eddy simulations of convective boundary layers using nonoscillatory differencing, Phys D Nonlin Phenom, 133, 390–397, https://doi.org/10.1016/S0167-2789(99)00083-4, 1999.

Mirocha, J. D., Kosović, B., Aitken, M. L., and Lundquist, J. K.: Implementation of a generalized actuator disk wind turbine model into the weather research and forecasting model for large-eddy simulation applications, J Renew Sust Energy, 6, 013 104, https://doi.org/10.1063/1.4861061, 2014.

Mühle, F., Adaramola, M. S., and Sætran, L.: The effect of rotational direction on the wake of a wind turbine rotor–a comparison study of aligned co-and counter rotating turbine arrays, Energy Procedia, 137, 238–245, https://doi.org/10.1016/j.egypro.2017.10.346, 2017.

Prusa, J. M., Smolarkiewicz, P. K., and Wyszogrodzki, A. A.: EULAG, a computational model for multiscale flows, Computers & Fluids, 37, 1193–1207, https://doi.org/10.1016/j.compfluid.2007.12.001, 2008.

Rhodes, M. E. and Lundquist, J. K.: The effect of wind-turbine wakes on summertime US Midwest atmospheric wind profiles as observed with ground-based doppler lidar, Boundary-Layer Meteorol, 149, 85–103, https://doi.org/10.1007/s10546-013-9834-x, 2013.

Sanchez Gomez, M. and Lundquist, J. K.: The effect of wind direction shear on turbine performance in a wind farm in central Iowa, WESD, 2019a.

Sanchez Gomez, M. and Lundquist, J. K.: Influence of wind veer on wind turbine power production, Wind Energy Science, 2019b.

Sanderse, B.: Aerodynamics of wind turbine wakes, Energy Research Center of the Netherlands (ECN), ECN-E–09-016, Petten, The Netherlands, Tech. Rep, 5, 153, 2009.

Schmidt, H. and Schumann, U.: Coherent structure of the convective boundary layer derived from large-eddy simulations, J Fluid Mech, 200, 511–562, https://doi.org/10.1017/S0022112089000753, 1989.

Shapiro, A. and Fedorovich, E.: Analytical description of a nocturnal low-level jet, Quarterly Journal of the Royal Meteorological Society, 136, 1255–1262, 2010.

Shen, W. Z., Zakkam, V. A. K., Sørensen, J. N., and Appa, K.: Analysis of counter-rotating wind turbines, in: Journal of Physics: Conference Series, vol. 75, p. 012003, IOP Publishing, https://doi.org/10.1088/1742-6596/75/1/012003, 2007.

Smolarkiewicz, P. K. and Margolin, L. G.: On forward-in-time differencing for fluids: extension to a curviliniear framework, Mon Weather Rev, 121, 1847–1859, https://doi.org/10.1175/1520-0493(1993)121<1847:OFITDF>2.0.CO;2, 1993.

Smolarkiewicz, P. K. and Margolin, L. G.: MPDATA: A Finite-Difference Solver for Geophysical Flows, J Comput Phys, 140, 459–480, https://doi.org/10.1006/jcph.1998.5901, 1998.

Smolarkiewicz, P. K. and Prusa, J. M.: Towards mesh adaptivity for geophysical turbulence: continuous mapping approach, Int J Numer Meth Fl, 47, 789–801, https://doi.org/10.1002/fld.858, 2005.

Smolarkiewicz, P. K. and Pudykiewicz, J. A.: A class of semi-Lagrangian approximations for fluids, J Atmos Sci, 49, 2082–2096, https://doi.org/10.1175/1520-0469(1992)049<2082:ACOSLA>2.0.CO;2, 1992.

Smolarkiewicz, P. K. and Winter, C. L.: Pores resolving simulation of Darcy flows, J Comput Phys, 229, 3121–3133, https://doi.org/10.1016/j.jcp.2009.12.031, 2010.

Smolarkiewicz, P. K., Sharman, R., Weil, J., Perry, S. G., Heist, D., and Bowker, G.: Building resolving large-eddy simulations and comparison with wind tunnel experiments, J Comput Phys, 227, 633–653, https://doi.org/10.1016/j.jcp.2007.08.005, 2007.

Stull, R. B.: An Introduction of Boundary Layer Meteorology, Dordrecht, Kluwer Academic, 1988.

Vermeer, L., Sørensen, J. N., and Crespo, A.: Wind turbine wake aerodynamics, Progress in aerospace sciences, 39, 467–510, https://doi.org/10.1016/S0376-0421(03)00078-2, 2003.

Vollmer, L., Lee, J. C., Steinfeld, G., and Lundquist, J.: A wind turbine wake in changing atmospheric conditions: LES and lidar measurements, in: Journal of Physics: Conference Series, vol. 854, p. 012050, IOP Publishing, https://doi.org/10.1088/1742-6596/75/1/012003, 2017.

Wallace, J. M. and Hobbs, P. V.: Atmospheric science: an introductory survey, vol. 92, Elsevier, 2006.

Walter, K., Weiss, C. C., Swift, A. H., Chapman, J., and Kelley, N. D.: Speed and direction shear in the stable nocturnal boundary layer, Journal of Solar Energy Engineering, 131, 011 013, https://doi.org/10.1115/1.3035818, 2009.

Wedi, N. P. and Smolarkiewicz, P. K.: Extending Gal-Chen and Somerville terrain-following coordinate transformation on time-dependent curvilinear boundaries, J Comput Phys, 193, 1–20, https://doi.org/10.1016/j.jcp.2003.07.034, 2004.

Yuan, W., Tian, W., Ozbay, A., and Hu, H.: An experimental study on the effects of relative rotation direction on the wake interferences among tandem wind turbines, Science China Physics, Mechanics & Astronomy, 57, 935–949, 2014.

Zhang, W., Markfort, C. D., and Porté-Agel, F.: Near-wake flow structure downwind of a wind turbine in a turbulent boundary layer, Exp Fluids, 52, 1219–1235, https://doi.org/10.1007/s00348-011-1250-8, 2012.